

SPLIT REPRESENTATION OF ADAPTIVELY COMPRESSED POLARIZABILITY OPERATOR

DONG AN*, LIN LIN†, AND ZE XU‡

Abstract. The polarizability operator plays a central role in density functional perturbation theory and other perturbative treatment of first principle electronic structure theories. The cost of computing the polarizability operator generally scales as $\mathcal{O}(N_e^4)$ where N_e is the number of electrons in the system. The recently developed adaptively compressed polarizability operator (ACP) formulation [L. Lin, Z. Xu and L. Ying, Multiscale Model. Simul. 2017] reduces such complexity to $\mathcal{O}(N_e^3)$ in the context of phonon calculations with a large basis set for the first time, and demonstrates its effectiveness for model problems. In this paper, we improve the performance of the ACP formulation by splitting the polarizability into a near singular component that is statically compressed, and a smooth component that is adaptively compressed. The new split representation maintains the $\mathcal{O}(N_e^3)$ complexity, and accelerates nearly all components of the ACP formulation, including Chebyshev interpolation of energy levels, iterative solution of Sternheimer equations, and convergence of the Dyson equations. For simulation of real materials, we discuss how to incorporate nonlocal pseudopotentials and finite temperature effects. We demonstrate the effectiveness of our method using one-dimensional model problem in insulating and metallic regimes, as well as its accuracy for real molecules and solids.

Key words. Density functional perturbation theory, phonon calculations, vibration properties, adaptive compression, split representation, polarizability operator, Sternheimer equation, Dyson equation.

AMS subject classifications. 65F10,65F30,65Z05

1. Introduction. Density functional perturbation theory (DFPT) [4, 17, 3, 9] studies the response of a quantum system under small perturbation, where the quantum system is described at the level of first principle electronic structure theories such as Kohn-Sham density functional theory (KSDFPT) [19, 23]. One important application of DFPT is the calculation of vibration properties such as phonons, which can be further used to calculate many physical properties such as infrared spectroscopy, elastic neutron scattering, specific heat, heat conduction, and electron-phonon interaction related behaviors such as superconductivity (see [3] for a review). DFPT describes vibration properties through a polarizability operator, which characterizes the linear response of the electron density with respect to the perturbation of the external potential. More specifically, in vibration calculations, the polarizability operator needs to be applied to $d \times N_A \sim \mathcal{O}(N_e)$ perturbation vectors, where d is the spatial dimension (usually $d = 3$), N_A is the number of atoms, and N_e is the number of electrons. In general the complexity for solving KSDFPT is $\mathcal{O}(N_e^3)$, while the complexity for solving DFPT is $\mathcal{O}(N_e^4)$. It is possible to reduce the computational complexity of DFPT calculations by “linear scaling methods” [16, 35, 6]. Such methods can be successful in reducing the computational cost for systems of large sizes with substantial band gaps, but this can be challenging for medium-sized systems with relatively small band gaps.

*Department of Mathematics, University of California, Berkeley, Berkeley, CA 94720. Email: dong_an@berkeley.edu

†Department of Mathematics, University of California, Berkeley, Berkeley, CA 94720 and Computational Research Division, Lawrence Berkeley National Laboratory, Berkeley, CA 94720. Email: linlin@math.berkeley.edu

‡Department of Mathematics, University of California, Berkeley, Berkeley, CA 94720. Email: zexu@math.berkeley.edu

The term “phonon calculation” usually describes the calculation of vibration properties of condensed matter systems. In this paper, we slightly abuse this term to refer to calculations of vibration properties of general systems, including condensed matter systems as well as isolated molecule clusters, since such calculations share the same mathematical structure. In order to apply the polarizability operator to $\mathcal{O}(N_e)$ vectors, we need to solve $\mathcal{O}(N_e^2)$ coupled Sternheimer equations. On the other hand, when a constant number of degrees of freedom per electron is used, the size of the Hamiltonian matrix is only $\mathcal{O}(N_e)$. Hence asymptotically there is room to obtain a set of only $\mathcal{O}(N_e)$ “compressed perturbation vectors”, which encodes essentially all the information of the $\mathcal{O}(N_e^2)$ Sternheimer equations. The recently developed adaptively compressed polarizability operator (ACP) formulation [27] follows this route, and successfully reduces the computational complexity of phonon calculations to $\mathcal{O}(N_e^3)$ for the first time. The ACP formulation does not rely on exponential decay properties of the density matrix as in linear scaling methods, and its accuracy depends weakly on the size of the band gap. Hence the method can be used for phonon calculations of both insulators and semiconductors with small gaps.

There are three key ingredients of the ACP formulation. 1) The Sternheimer equations are equations for shifted Hamiltonians, where each shift corresponds to an energy level of an occupied band. Hence for a general right hand side vector, there are N_e possible energies (shifts). We use a Chebyshev interpolation procedure to disentangle such energy dependence so that there are only constant number of shifts that is independent of N_e . 2) We disentangle the $\mathcal{O}(N_e^2)$ right hand side vectors in the Sternheimer equations using the recently developed interpolative separable density fitting procedure, to compress the right-hand-side vectors. 3) We construct the polarizability operator by adaptive compression so that the operator remains low rank as well as accurate when applying to a certain set of vectors. This make it possible for fast computation of the matrix inversion using methods like Sherman-Morrison-Woodbury. In particular, the ACP method does not employ the “nearsightedness” property of electrons for insulating systems with substantial band gaps as in linear scaling methods [22]. Hence the ACP method can be applied to insulators as well as semiconductors with small band gaps.

In this paper, we introduce a generalization the ACP formulation for efficient phonon calculations of real materials called split representation of ACP. In the split representation, the nonlocal pseudopotential is taken into account, as well as temperature effects especially for metallic systems. The new split representation maintains the $\mathcal{O}(N_e^3)$ complexity, and improves all key steps in the ACP formulation, including Chebyshev interpolation of energy levels, iterative solution of Sternheimer equations, and convergence of the Dyson equations.

The rest of the paper is organized as follows. Section 2 introduces the basic formulation of KSDFT and DFPT, and reviews the formulation of ACP. Section 3 describes the split representation of the ACP formulation. Numerical results are presented in section 4, followed by conclusion and discussion in section 5.

2. Preliminaries.

2.1. Kohn-Sham density functional theory. For simplicity we consider a system of finite size with periodic boundary conditions. This can be used to model isolated molecular systems as well as solid state systems with the Gamma point sampling strategy of the Brillouin zone [30]. However, we do not explicitly take advantage of that $\{\psi_i(\mathbf{r})\}$ are real, so that the formulation is applicable to real space and Fourier space implementation, as commonly done in electronic structure software packages.

The spatial dimension $d = 3$ is assumed in the treatment of e.g. Coulomb interaction unless otherwise specified. Since our numerical results involve real materials and systems of both insulating and metallic characters, we include relevant technical details such as nonlocal pseudopotential and temperature dependence in the discussion. Consider a system consisting of N_A nuclei and N_e electrons at temperature $T = 1/(k_B\beta)$, where k_B is the Boltzmann constant. In the Born-Oppenheimer approximation, for each set of nuclear positions $\{\mathbf{R}_I\}_{I=1}^{N_A}$, the electrons are relaxed to their ground state. The ground state total energy is denoted by $E_{\text{tot}}(\{\mathbf{R}_I\}_{I=1}^{N_A})$, and can be computed in Kohn-Sham density functional theory [19, 23, 31] according to the minimization of the following Kohn-Sham-Mermin energy functional

$$\begin{aligned}
& E_{\text{KS}}(\{\psi_i\}; \{\mathbf{R}_I\}) \\
&= \frac{1}{2} \sum_{i=1}^{\infty} f_i \int |\nabla \psi_i(\mathbf{r})|^2 d\mathbf{r} + \sum_{i=1}^{\infty} f_i \int \psi_i^*(\mathbf{r}) V_{\text{ion}}(\mathbf{r}, \mathbf{r}'; \{\mathbf{R}_I\}) \psi_i(\mathbf{r}') d\mathbf{r} d\mathbf{r}' \\
&+ \frac{1}{2} \iint v_c(\mathbf{r}, \mathbf{r}') \rho(\mathbf{r}) \rho(\mathbf{r}') d\mathbf{r} d\mathbf{r}' + E_{\text{xc}}[\rho] + E_{\text{II}}(\{\mathbf{R}_I\}) \\
&+ \frac{1}{\beta} \sum_{i=1}^{\infty} [f_i \log f_i + (1 - f_i) \log(1 - f_i)].
\end{aligned} \tag{2.1}$$

Here the minimization is with respect to the Kohn-Sham orbitals $\{\psi_i\}_{i=1}^{\infty}$ satisfying the orthonormality condition $\int \psi_i^*(\mathbf{r}) \psi_j(\mathbf{r}) d\mathbf{r} = \delta_{ij}$, as well as the occupation numbers $\{f_i\}_{i=1}^{\infty}$ satisfying $0 \leq f_i \leq 1$. In Eq. (2.1), $\rho(\mathbf{r}) = \sum_{i=1}^{\infty} f_i |\psi_i(\mathbf{r})|^2$ defines the electron density with normalization condition $\int \rho(\mathbf{r}) d\mathbf{r} = N_e$. In the discussion below we will omit the range of indices I, i unless otherwise specified. In Eq. (2.1), $v_c(\mathbf{r}, \mathbf{r}') = \frac{1}{|\mathbf{r} - \mathbf{r}'|}$ defines the kernel for Coulomb interaction in \mathbb{R}^3 and the corresponding term is called the Hartree energy. V_{ion} is a potential characterizing the electron-ion interaction, and is independent of the electronic states $\{\psi_i\}$. More specifically, in a pseudopotential approximation [30], if we view V_{ion} as an integral operator, then the kernel of V_{ion} can be expressed as the summation of contribution from each atom I

$$V_{\text{ion}}(\mathbf{r}, \mathbf{r}'; \{\mathbf{R}_I\}) = \sum_I V_{\text{loc},I}(\mathbf{r} - \mathbf{R}_I) \delta(\mathbf{r} - \mathbf{r}') + \sum_I V_{\text{nl},I}(\mathbf{r} - \mathbf{R}_I, \mathbf{r}' - \mathbf{R}_I). \tag{2.2}$$

Here $V_{\text{loc},I}$ is called the local pseudopotential, and $V_{\text{nl},I}$ the nonlocal pseudopotential. In the Kleinman-Bylander form [20], each nonlocal pseudopotential is a low rank and symmetric operator with kernel

$$V_{\text{nl},I}(\mathbf{r} - \mathbf{R}_I, \mathbf{r}' - \mathbf{R}_I) = \sum_{l=1}^{L_I} \gamma_{I,l} b_{I,l}(\mathbf{r} - \mathbf{R}_I) b_{I,l}^*(\mathbf{r}' - \mathbf{R}_I). \tag{2.3}$$

Here $\gamma_{I,l}$ is a weight factor, and each $b_{I,l}$ is a real valued function. The function $b_{I,l}$ is also localized, in the sense that it is compactly supported around $\mathbf{r} = 0$. The locality originates from the physical meaning of nonlocal pseudopotentials, i.e. they characterize the orthogonality of the valence electron orbitals with respect to the core electron orbitals, and hence the support of $b_{I,l}$ is restricted by the span of the core orbitals. E_{xc} is the exchange-correlation energy, and here we assume semi-local functionals such as local density approximation (LDA) [10, 39] and generalized gradient approximation (GGA) functionals [5, 24, 38] are used. E_{II} is the ion-ion Coulomb interaction energy. For isolated clusters in 3D, $E_{\text{II}}(\{\mathbf{R}_I\}) = \frac{1}{2} \sum_{I \neq J} \frac{Z_I Z_J}{|\mathbf{R}_I - \mathbf{R}_J|}$, while for

periodic systems the contribution from all the image charges should be properly taken into account via e.g. the Ewald summation technique [14]. The last term of Eq. (2.1) is the entropy term related to the temperature, and spin degeneracy is neglected for simplicity of the notation.

The Euler-Lagrange equation associated with the Kohn-Sham energy functional gives rise to the Kohn-Sham equations as

$$H[\rho]\psi_i = \left(-\frac{1}{2}\Delta + \mathcal{V}[\rho]\right)\psi_i = \varepsilon_i\psi_i, \quad (2.4)$$

$$\int \psi_i^*(\mathbf{r})\psi_j(\mathbf{r})\mathbf{d}\mathbf{r} = \delta_{ij}, \quad \rho(\mathbf{r}) = \sum_{i=1}^{\infty} f_i |\psi_i(\mathbf{r})|^2, \quad f_i = \frac{1}{1 + e^{\beta(\varepsilon_i - \mu)}}. \quad (2.5)$$

Here the eigenvalues $\{\varepsilon_i\}$ are ordered non-decreasingly. Note that the occupation number f_i is given analytically by the Fermi-Dirac distribution with respect to the eigenvalue ε_i , and μ is a Lagrange multiplier enforcing the normalization condition of the electron density. The difference of the eigenvalues $\varepsilon_g = \varepsilon_{N_e+1} - \varepsilon_{N_e}$ is called the energy gap. If ε_g is positive, then the system is called an insulating system. Otherwise it is a metallic system. For insulating systems, $\psi_1, \dots, \psi_{N_e}$ are called the occupied orbitals, while ψ_{N_e+1}, \dots are called the unoccupied orbitals. ψ_{N_e} is sometimes called the highest occupied molecular orbital (HOMO), and ψ_{N_e+1} the lowest unoccupied molecular orbital (LUMO).

The effective potential $\mathcal{V}[\rho]$ depends on the electron density ρ as

$$\mathcal{V}[\rho](\mathbf{r}, \mathbf{r}') = V_{\text{ion}}(\mathbf{r}, \mathbf{r}') + \left[\int v_c(\mathbf{r}, \mathbf{r}')\rho(\mathbf{r}')\mathbf{d}\mathbf{r}' + V_{\text{xc}}[\rho](\mathbf{r}) \right] \delta(\mathbf{r} - \mathbf{r}'). \quad (2.6)$$

Here $V_{\text{xc}}[\rho](\mathbf{r}) = \frac{\delta E_{\text{xc}}}{\delta \rho(\mathbf{r})}$ is the exchange-correlation potential, which is the functional derivative of the exchange-correlation energy with respect to the electron density. The Kohn-Sham Hamiltonian depends nonlinearly on the electron density ρ , and the electron density should be solved self-consistently. When the Kohn-Sham energy functional E_{KS} achieves its minimum, the self-consistency of the electron density is simultaneously achieved. Note that both the Hartree potential and the exchange-correlation potential are local potentials. This plays an important role in simplifying the treatment of the density functional perturbation theory.

When the Kohn-Sham energy functional E_{KS} achieves its minimum, the self-consistency of the electron density is simultaneously achieved. Then the total energy can be equivalently computed as [30]

$$E_{\text{tot}} = \sum_{i=1}^{N_e} \varepsilon_i - \frac{1}{2} \iint v_c(\mathbf{r}, \mathbf{r}')\rho(\mathbf{r})\rho(\mathbf{r}')\mathbf{d}\mathbf{r}\mathbf{d}\mathbf{r}' - \int V_{\text{xc}}[\rho](\mathbf{r})\rho(\mathbf{r})\mathbf{d}\mathbf{r} + E_{\text{xc}}[\rho] + E_{\text{II}}(\{\mathbf{R}_I\}). \quad (2.7)$$

Here $E_{\text{band}} = \sum_{i=1}^{N_e} \varepsilon_i$ is referred to as the band energy.

At this point, the atomic force can be given by the negative of the first order derivative of E_{tot} with respect to the atomic configuration using the Hellmann-Feynman theorem as

$$\mathbf{F}_I = -\frac{\partial E_{\text{tot}}(\{\mathbf{R}_I\})}{\partial \mathbf{R}_I} = -\int \frac{\partial V_{\text{ion}}(\mathbf{r}, \mathbf{r}'; \{\mathbf{R}_I\})}{\partial \mathbf{R}_I} P(\mathbf{r}', \mathbf{r})\mathbf{d}\mathbf{r}\mathbf{d}\mathbf{r}' - \frac{\partial E_{\text{II}}(\{\mathbf{R}_I\})}{\partial \mathbf{R}_I}. \quad (2.8)$$

Here P is the density matrix defined as

$$P(\mathbf{r}, \mathbf{r}') = \sum_{i=1}^{\infty} f_i \psi_i(\mathbf{r}) \psi_i^*(\mathbf{r}'). \quad (2.9)$$

In particular, the diagonal entries of the density matrix $P(\mathbf{r}, \mathbf{r})$ is the electron density $\rho(\mathbf{r})$. The derivative of the pseudopotential $\frac{\partial V_{\text{ion}}}{\partial \mathbf{R}_I}(\mathbf{r}, \mathbf{r}'; \{\mathbf{R}_I\})$ does not depend on the electron density, can be obtained semi-analytically. Hence the computation of the atomic force only involves a number of quadratures. The atomic force allows the performance of structural relaxation of the atomic configuration, by minimizing the total energy E_{tot} with respect to the atomic positions $\{\mathbf{R}_I\}$. When the atoms are at their equilibrium positions, all atomic forces should be zero.

2.2. Density functional perturbation theory. In density functional perturbation theory (DFPT), we assume that the self-consistent ground state electron density ρ has been computed, denoted by ρ^* . In this paper, we focus on phonon calculations using DFPT. Assume the system deviates from its equilibrium position $\{\mathbf{R}_I\}$ by some small magnitude, then the changes of the total energy is dominated by the Hessian matrix with respect to the atomic positions. The dynamical matrix D consists of $d \times d$ blocks in the form

$$D_{I,J} = \frac{1}{\sqrt{M_I M_J}} \frac{\partial^2 E_{\text{tot}}(\{\mathbf{R}_I\})}{\partial \mathbf{R}_I \partial \mathbf{R}_J},$$

where M_I is the mass of the I -th nuclei. The dimension of the dynamical matrix is $d \times N_A$. The equilibrium atomic configuration is at a local minimum of the total energy, and all the eigenvalues of D are real and non-negative. Hence the eigen-decomposition of D is

$$D u_k = \omega_k^2 u_k,$$

where u_k is called the k -th phonon mode, and ω_k is called the k -th phonon frequency. The phonon spectrum is defined as the distribution of the eigenvalues $\{\omega_k\}$ i.e.

$$\varrho_D(\omega) = \frac{1}{dN_A} \sum_k \delta(\omega - \omega_k). \quad (2.10)$$

Here δ is the Dirac- δ distribution. ϱ_D is also referred to as the density of states of D [30, 26].

In order to compute the Hessian matrix, we obtain from Eq. (2.8) that

$$\begin{aligned} \frac{\partial^2 E_{\text{tot}}(\{\mathbf{R}_I\})}{\partial \mathbf{R}_I \partial \mathbf{R}_J} &= \int \frac{\partial V_{\text{ion}}}{\partial \mathbf{R}_I}(\mathbf{r}, \mathbf{r}'; \{\mathbf{R}_I\}) \frac{\partial P(\mathbf{r}', \mathbf{r})}{\partial \mathbf{R}_J} \mathbf{dr} \mathbf{dr}' \\ &+ \int \frac{\partial^2 V_{\text{ion}}}{\partial \mathbf{R}_I \partial \mathbf{R}_J}(\mathbf{r}, \mathbf{r}'; \{\mathbf{R}_I\}) P(\mathbf{r}', \mathbf{r}) \mathbf{dr} \mathbf{dr}' + \frac{\partial^2 E_{\text{II}}(\{\mathbf{R}_I\})}{\partial \mathbf{R}_I \partial \mathbf{R}_J}. \end{aligned} \quad (2.11)$$

Similar to the force calculation, the second term of Eq. (2.11) can be readily computed with numerical integration, and the third term involves only ion-ion interaction that is independent of the electronic states. Hence the first term is the most challenging one due to the response of the electron density with respect to the perturbation

of atomic positions. Applying the chain rule, we have

$$\begin{aligned} & \int \frac{\partial V_{\text{ion}}(\mathbf{r}, \mathbf{r}'; \{\mathbf{R}_I\})}{\partial \mathbf{R}_I} \frac{\partial P(\mathbf{r}', \mathbf{r})}{\partial \mathbf{R}_J} d\mathbf{r} d\mathbf{r}' \\ &= \int \frac{\partial V_{\text{ion}}(\mathbf{r}, \mathbf{r}'; \{\mathbf{R}_I\})}{\partial \mathbf{R}_I} \frac{\delta P(\mathbf{r}', \mathbf{r})}{\delta V_{\text{ion}}(\mathbf{r}'', \mathbf{r}''')} \frac{\partial V_{\text{ion}}(\mathbf{r}'', \mathbf{r}'''); \{\mathbf{R}_I\}}{\partial \mathbf{R}_J} d\mathbf{r} d\mathbf{r}' d\mathbf{r}'' d\mathbf{r}'''. \end{aligned} \quad (2.12)$$

Here the Fréchet derivative $\mathfrak{X}(\mathbf{r}, \mathbf{r}'; \mathbf{r}'', \mathbf{r}''') = \frac{\delta P(\mathbf{r}, \mathbf{r}')}{\delta V_{\text{ion}}(\mathbf{r}'', \mathbf{r}''')}$ is referred to as the reducible polarizability operator [36], which characterizes the *self-consistent* linear response of the density matrix at $(\mathbf{r}, \mathbf{r}')$ with respect to an external nonlocal perturbation of V_{ion} at $(\mathbf{r}'', \mathbf{r}''')$. However, the computation of \mathfrak{X} must be obtained through a simpler quantity $\mathfrak{X}_0(\mathbf{r}, \mathbf{r}'; \mathbf{r}'', \mathbf{r}''') = \frac{\delta P(\mathbf{r}, \mathbf{r}')}{\delta \mathcal{V}(\mathbf{r}'', \mathbf{r}''')}$, which is called the irreducible polarizability operator (a.k.a. independent particle polarizability operator) [36].

The discussion using the notation $\mathbf{r}, \mathbf{r}', \mathbf{r}''$ etc will quickly become complicated. For simplicity in the discussion below, we will not distinguish the continuous and discretized representations of various quantities. In the case when a discretized representation is needed, we assume that the computational domain is uniformly discretized into a number of grid points $\{\mathbf{r}_\alpha\}_{\alpha=1}^{N_g}$. After discretization all quantities can be called tensors. For example, we will call $u(\mathbf{r})$ an order 1 tensor (or a vector), $A(\mathbf{r}, \mathbf{r}')$ an order 2 tensor (or a matrix), and $\mathfrak{X}(\mathbf{r}, \mathbf{r}'; \mathbf{r}'', \mathbf{r}''')$ an order 4 tensor. The tensor slicing and tensor contraction can be denoted using either the continuous or the discrete notation. For example, $\mathfrak{X}(\mathbf{r}, \mathbf{r}; \mathbf{r}'', \mathbf{r}''')$ denotes a sliced tensor which is an order 3 tensor. The tensor contraction between two order 1 tensors u and v should be interpreted as $u^*v = \int u^*(\mathbf{r})v(\mathbf{r})d\mathbf{r}$. The tensor contraction between an order 2 tensor A and an order 1 tensor v (i.e. a matrix-vector product) should be interpreted as $(Av)(\mathbf{r}) = \int A(\mathbf{r}, \mathbf{r}')v(\mathbf{r}')d\mathbf{r}'$. Similarly the contraction between an order 2 tensor A and an order 2 tensor \mathbf{g} (i.e. matrix-matrix product) should be interpreted as $(A\mathbf{g})(\mathbf{r}, \mathbf{r}') = \int A(\mathbf{r}, \mathbf{r}'')\mathbf{g}(\mathbf{r}'', \mathbf{r}')d\mathbf{r}''$, and the contraction between an order 4 tensor \mathfrak{X} and an order 2 tensor \mathbf{g} should be interpreted as

$$(\mathfrak{X}\mathbf{g})(\mathbf{r}, \mathbf{r}') = \int \mathfrak{X}(\mathbf{r}, \mathbf{r}'; \mathbf{r}'', \mathbf{r}''')\mathbf{g}(\mathbf{r}'', \mathbf{r}''')d\mathbf{r}'' d\mathbf{r}'''.$$

We also define two operations for order 1 tensors. The Hadamard product of two order 1 tensors $u \odot v$ should be interpreted as $(u \odot v)(\mathbf{r}) := u(\mathbf{r})v(\mathbf{r})$. For an order 1 tensor $v(\mathbf{r})$, we define an associated order 2 tensor as $(\text{diag}[v])(\mathbf{r}, \mathbf{r}') := v(\mathbf{r})\delta(\mathbf{r} - \mathbf{r}')$. It is easy to verify that the Hadamard product can be written as $u \odot v = \text{diag}[u]v$.

Using the linear algebra type of notation as above, the key difficulty of phonon calculations is the computation of the tensor contraction $\mathbf{u} = \mathfrak{X}\mathbf{g}$, where \mathbf{g} traverses $d \times N_A$ order 2 tensors of the form $\frac{\partial V_{\text{ion}}(\mathbf{r}'', \mathbf{r}'''); \{\mathbf{R}_I\}}{\partial \mathbf{R}_{J,a}}$, where $\mathbf{R}_{J,a}$ is the a -th direction of the atomic position \mathbf{R}_J ($a = 1, \dots, d$). According to Eq. (2.2), \mathbf{g} can split into a local component and a nonlocal component as

$$\mathbf{g}(\mathbf{r}, \mathbf{r}') = g_{\text{loc}}(\mathbf{r})\delta(\mathbf{r} - \mathbf{r}') + \mathbf{g}_{\text{nl}}(\mathbf{r}, \mathbf{r}'), \quad (2.13)$$

or equivalently $\mathbf{g} = \text{diag}[g_{\text{loc}}] + \mathbf{g}_{\text{nl}}$. For each \mathbf{g} , only one atom J contributes to the order 1 tensor g_{loc} and the order 2 tensor \mathbf{g}_{nl} . From the definition of nonlocal

pseudopotential Eq. (2.3), we have

$$\mathbf{g}_{\text{nl},I}(\mathbf{r}, \mathbf{r}') = \sum_{l=1}^{L_I} \gamma_{I,l} [b_{I,l}(\mathbf{r} - \mathbf{R}_I) db_{I,l}^*(\mathbf{r}' - \mathbf{R}_I) + db_{I,l}(\mathbf{r} - \mathbf{R}_I) b_{I,l}^*(\mathbf{r}' - \mathbf{R}_I)],$$

where $db_{I,l}(\mathbf{r} - \mathbf{R}_I) := \frac{\partial b_{I,l}(\mathbf{r} - \mathbf{R}_I)}{\partial \mathbf{R}_I}$.

(2.14)

We note that \mathbf{g}_{nl} is a symmetric operator of rank $2L_I$, where the factor 2 comes from the Leibniz formula. In the rest of the paper, we shall use $b_l(\mathbf{r}), db_l(\mathbf{r})$ to hide the explicit dependence on the atom indices I or the atomic positions $\{\mathbf{R}_I\}$.

From the definition of \mathcal{V} in Eq. (2.6), we apply the chain rule and have

$$\mathbf{u} = \mathfrak{X}\mathbf{g} = \frac{\delta P}{\delta \mathcal{V}} \frac{\delta \mathcal{V}}{\delta V_{\text{ion}}} \mathbf{g} = \mathfrak{X}_0 \mathbf{g} + \mathfrak{X}_0 f_{\text{hxc}} \mathfrak{X} \mathbf{g} = \mathfrak{X}_0 \mathbf{g} + \mathfrak{X}_0 f_{\text{hxc}} \mathbf{u}. \quad (2.15)$$

In Eq. (2.15),

$$\begin{aligned} f_{\text{hxc}}(\mathbf{r}, \mathbf{r}'; \mathbf{r}'', \mathbf{r}''') &= \left(v_c(\mathbf{r}, \mathbf{r}'') + \frac{\delta V_{\text{xc}}[\rho^*](\mathbf{r})}{\delta \rho(\mathbf{r}'')} \right) \delta(\mathbf{r} - \mathbf{r}') \delta(\mathbf{r}'' - \mathbf{r}''') \\ &:= f_{\text{hxc}}(\mathbf{r}, \mathbf{r}'') \delta(\mathbf{r} - \mathbf{r}') \delta(\mathbf{r}'' - \mathbf{r}''') \end{aligned} \quad (2.16)$$

is an order 4 tensor, which is the kernel characterizing the dependence of the \mathcal{V} with respect to the density matrix P in the linear regime. Here $\frac{\delta V_{\text{xc}}[\rho^*](\mathbf{r})}{\delta \rho(\mathbf{r}'')}$ is called the exchange-correlation kernel, which is a local operator in the LDA and GGA formulations of the exchange-correlation functionals. Therefore in Eq. (2.16), $\delta(\mathbf{r} - \mathbf{r}')$ comes from that the Hartree and exchange-correlation potentials are local, while $\delta(\mathbf{r}'' - \mathbf{r}''')$ comes from that the nonlinear term only depends on the electron density, i.e. the diagonal elements of the density matrix. Eq. (2.15) is called the *Dyson equation*, and the solution \mathbf{u} should be solved self-consistently.

In order to solve the Dyson equation (2.15), we need to apply \mathfrak{X}_0 to order 2 tensors of the form \mathbf{g} or $f_{\text{hxc}}\mathbf{u}$. By means of the eigenfunctions ψ_i , the eigenvalues ε_i , and the occupation numbers f_i , $\mathfrak{X}_0 \mathbf{g}$ can be expressed using the Adler-Wiser formula [1, 46]

$$(\mathfrak{X}_0 \mathbf{g})(\mathbf{r}, \mathbf{r}') = \sum_{i,a=1}^{\infty} \frac{f_a - f_i}{\varepsilon_a - \varepsilon_i} \psi_a(\mathbf{r}) \left(\int \psi_a^*(\mathbf{r}'') \mathbf{g}(\mathbf{r}'', \mathbf{r}''') \psi_i(\mathbf{r}''') d\mathbf{r}'' d\mathbf{r}''' \right) \psi_i^*(\mathbf{r}'), \quad (2.17)$$

where the term when $i = a$ should be interpreted as the limit when $\varepsilon_a \rightarrow \varepsilon_i$. Using the linear algebra notation, Eq. (2.17) can be written as

$$\mathfrak{X}_0 \mathbf{g} = \sum_{i,a=1}^{\infty} \frac{f_a - f_i}{\varepsilon_a - \varepsilon_i} \psi_a (\psi_a^* \mathbf{g} \psi_i) \psi_i^*. \quad (2.18)$$

Since \mathbf{g} is an Hermitian order 2 tensor, $\mathfrak{X}_0 \mathbf{g}$ is also an Hermitian order 2 tensor. If we truncate the infinite sum in Eq. (2.18) to a finite sum of states, Eq. (2.18) and Eq. (2.15) can be solved together to obtain \mathbf{u} , and therefore the Hessian matrix (2.11) can be evaluated.

In order to observe the computational complexity of DFPT for phonon calculations, let us first neglect the nonlocal pseudopotential $V_{\text{nl},I}$, which simplifies the

discussion. Since each \mathbf{g} only involves the local contribution, Eq. (2.11) only requires $\frac{\partial \rho(\mathbf{r})}{\partial \mathbf{R}_J}$. Therefore one is only interested in computing

$$u(\mathbf{r}) = \mathbf{u}(\mathbf{r}, \mathbf{r}) = \int \mathfrak{X}(\mathbf{r}, \mathbf{r}; \mathbf{r}', \mathbf{r}') \mathbf{g}(\mathbf{r}', \mathbf{r}') d\mathbf{r}' := \int \chi(\mathbf{r}, \mathbf{r}') g_{\text{loc}}(\mathbf{r}') d\mathbf{r}'. \quad (2.19)$$

Here we have introduced the notation $\chi(\mathbf{r}, \mathbf{r}') = \mathfrak{X}(\mathbf{r}, \mathbf{r}; \mathbf{r}', \mathbf{r}')$, and used that the nonlocal component of \mathbf{g} vanishes. Similarly we can define $\chi_0(\mathbf{r}, \mathbf{r}') = \mathfrak{X}_0(\mathbf{r}, \mathbf{r}; \mathbf{r}', \mathbf{r}')$. We also consider insulating systems with a finite band gap. This allows us to reduce the temperature dependence of the occupation number, so that $f_i = 1$ if $i \leq N_e$ and 0 if $i \geq N_e + 1$. As a result, Eq. (2.18) can be simplified as

$$\chi_0 g_{\text{loc}} = \sum_{i=1}^{N_e} \sum_{a=N_e+1}^{\infty} \frac{1}{\varepsilon_i - \varepsilon_a} \text{diag}[\psi_i^*] \psi_a (\psi_a^* \text{diag}[g_{\text{loc}}] \psi_i) + \text{h.c.} \quad (2.20)$$

Here h.c. means the Hermitian conjugate of the first term.

In order to overcome the difficulty of explicitly computing all the unoccupied orbitals $\{\psi_a\}_{a=N_e+1}^{\infty}$, we first define the projection operator to the unoccupied space $Q = I - \sum_{i=1}^{N_e} \psi_i \psi_i^*$. Then we can compute $\chi_0 g_{\text{loc}}$ as

$$\chi_0 g_{\text{loc}} = \sum_{i=1}^{N_e} \text{diag}[\psi_i^*] Q (\varepsilon_i - H)^{-1} Q (\text{diag}[g_{\text{loc}}] \psi_i) + \text{h.c.} \quad (2.21)$$

In principle, since Q commutes with H , the right hand side of Eq. (2.21) only requires one Q operator to be present. However, we choose the form $Q(\varepsilon_i - H)^{-1}Q$ to emphasize that this operator is Hermitian. Let $\zeta_i := Q(\varepsilon_i - H)^{-1}Q(\text{diag}[g_{\text{loc}}]\psi_i)$, the matrix inverse in Eq. (2.21) can be avoided by solving the *Sternheimer equations*

$$Q(\varepsilon_i - H)Q\zeta_i = Q(\text{diag}[g_{\text{loc}}]\psi_i). \quad (2.22)$$

This strategy has been used in a number of contexts involving the polarizability operator [17, 36, 44, 15, 34]. The Sternheimer equations can be solved using standard direct or iterative linear solvers. The choice of the solver can depend on practical matters such as the discretization scheme, and the availability of preconditioners. In practice for planewave discretization, we find that the use of the minimal residual method (MINRES) [37] gives the best numerical performance.

The complexity of phonon calculations can now be analyzed as below. Even with local pseudopotential only, and assume the Dyson equations always converge within a constant number of iterations that is independent of the system size N_e , we need to apply χ_0 to $d \times N_A \sim \mathcal{O}(N_e)$ vectors of the form g_{loc} . Each g_{loc} requires solving N_e Sternheimer equations (2.22), and the computational cost of applying the projection operator Q to a vector is $\mathcal{O}(N_e^2)$. Hence the overall complexity is $\mathcal{O}(N_e^4)$ [3]. This is significantly more expensive than solving the KSDFE, of which the computational complexity is typically $\mathcal{O}(N_e^3)$.

2.3. Adaptively compressed polarizability operator. In this section we briefly review the ACP formulation [27] in the context of phonon calculations for insulating systems using local pseudopotentials. If we label the possible g_{loc} using a single index j , the Sternheimer equation (2.22) can be written as

$$Q(\varepsilon_i - H)Q\zeta_{ij} = Q(\psi_i \odot g_{\text{loc},j}). \quad (2.23)$$

Here we have used the relation $\text{diag}[g_{\text{loc}}]\psi = \psi \odot g_{\text{loc}}$ to place g_{loc} and ψ on a more symmetric footing. Then reduction of the computational complexity is achieved by means of reducing the $\mathcal{O}(N_e^2)$ equations in Eq. (2.23) to $\mathcal{O}(N_e)$ equations with systematic control of the accuracy.

The compression of the right hand side vectors is performed via the interpolative separable density fitting method by Lu and Ying [29]. Let us denote by M the collection of right hand side vectors in Eq. (2.23) without the Q factor, i.e. $M_{ij} = \psi_i \odot g_{\text{loc},j}$. Here we have used ij as a stacked column index for the matrix M . The dimension of M is $N_g \times \mathcal{O}(N_e^2)$. Due to the large number of columns of M , we seek for the following interpolative decomposition (ID) type of compression [12] for the matrix M , i.e.

$$M_{ij}(\mathbf{r}) \approx \sum_{\mu=1}^{N_\mu} \xi_\mu(\mathbf{r}) M_{ij}(\mathbf{r}_\mu) \equiv \sum_{\mu=1}^{N_\mu} \xi_\mu(\mathbf{r}) \psi_i(\mathbf{r}_\mu) g_{\text{loc},j}(\mathbf{r}_\mu). \quad (2.24)$$

Here $\{\mathbf{r}_\mu\}_{\mu=1}^{N_\mu}$ denotes a collection of selected row indices (see Fig. 1 in [27] for an illustration). Mathematically, the meaning of the indices $\{\mathbf{r}_\mu\}$ is clear: Eq. (2.24) simply states that for any grid point \mathbf{r} , the corresponding row vector $M_i(\mathbf{r})$ can be approximately expressed as the linear combination of the selected rows $\{M_i(\mathbf{r}_\mu)\}$. Since $N_g \sim N_e$, as N_e increases, the column dimension of M (which is $\mathcal{O}(N_e^2)$) can be larger than its row dimension (which is N_g), and we can expect that the vectors $\{\psi_i \odot g_j\}$ are approximately linearly dependent. Such observation has been observed in the electronic structure community under the name of density fitting or resolution of identity (RI) [45, 41, 13, 43, 40], and the numerical rank of the matrix M after truncation can be only $\mathcal{O}(N_e)$ with a relatively small pre-constant. This dimension reduction property has also been recently analyzed in [28]. In the context of the interpolative decomposition, our numerical results also indicate that it is sufficient to choose $N_\mu \sim \mathcal{O}(N_e)$, and the pre-constant is small.

One possible way of finding interpolative decomposition is to use a pivoted QR factorization [11, 18]. However, the computational complexity for compressing the dense matrix M using the interpolative decomposition is still $\mathcal{O}(N_e^4)$. The interpolative separable density fitting method [29] employs a two-step procedure to reduce this cost. The first step is to use a fast down-sampling procedure, such as a subsampled random Fourier transform (SRFT) [47], to transform the matrix M into a matrix \widetilde{M} of smaller dimension $N_g \times rN_e$, with r a relatively small constant so that rN_e is slightly larger than N_μ . The second step is to apply the pivoted QR decomposition to \widetilde{M}

$$\widetilde{M}^* \widetilde{\Pi} = \widetilde{Q} \widetilde{R}, \quad (2.25)$$

where $\widetilde{\Pi}$ is a permutation matrix and encodes the choice of the row indices $\{\mathbf{r}_\mu\}$ from \widetilde{M} . The interpolation vectors $\{\xi_\mu\}$ in Eq. (2.24) can be also be computed from this pivoted QR decomposition. It should be noted that the pre-processing procedure does not affect the quality of the interpolative decomposition, while the cost of the pivoted QR factorization in Eq. (2.25) is now reduced to $\mathcal{O}(N_g N_\mu^2) \sim \mathcal{O}(N_e^3)$. We refer readers to [29, 27] for a more detailed description of this procedure.

Once the compressed representation (2.24) is obtained, we solve the following set of modified Sternheimer equations

$$Q(\varepsilon_i - H)Q\widetilde{\zeta}_{c\mu} = Q\xi_\mu, \quad i = 1, \dots, N_e, \quad \mu = 1, \dots, N_\mu.$$

Note that there are still $\mathcal{O}(N_e^2)$ equations to solve, but this time the number of equations arises from the energy dependence on the left hand side of the equation. If the band gap is positive, we can solve a set of equations of the form

$$Q(\tilde{\varepsilon}_c - H)Q\tilde{\zeta}_{c\mu} = Q\xi_\mu, \quad c = 1, \dots, N_c, \quad \mu = 1, \dots, N_\mu. \quad (2.26)$$

where the number of shifts N_c is independent of the system size N_e . For example, this can be achieved using the Chebyshev points on the occupied band $[\varepsilon_1, \varepsilon_{N_e}]$, and the number of Chebyshev points needed to achieve a certain error tolerance scales weakly with respect to the band gap as $\sqrt{|\mathcal{I}|/\varepsilon_g}$. Here ε_g is the band gap and $|\mathcal{I}| = \varepsilon_{N_e} - \varepsilon_1$ is the width of the occupied band [27].

Then define

$$W_\mu = \sum_{i=1}^{N_e} \text{diag}[\psi_i^*] \odot \left(\sum_{c=1}^{N_c} \tilde{\zeta}_{c\mu} \prod_{c' \neq c} \frac{\varepsilon_i - \tilde{\varepsilon}_{c'}}{\tilde{\varepsilon}_c - \tilde{\varepsilon}_{c'}} \right) \psi_i(\mathbf{r}_\mu) + \text{h.c.}, \quad (2.27)$$

and we can combine Eq. (2.27) with Eq. (2.22) to compute $\chi_0 g_{\text{loc},j}$ as

$$\chi_0 g_{\text{loc},j} \approx \sum_{\mu=1}^{N_\mu} W_\mu g_{\text{loc},j}(\mathbf{r}_\mu). \quad (2.28)$$

Formally, Eq. (2.28) can further be simplified by defining a matrix Π with N_μ columns, which consists of selected columns of a permutation matrix, i.e. $\Pi = \tilde{\Pi}_{:,1:N_\mu}$ as the first N_μ columns of the permutation matrix obtained from pivoted QR decomposition. More specifically, $\Pi_\mu = e_{\mathbf{r}_\mu}$ and $e_{\mathbf{r}_\mu}$ is a unit vector with only one nonzero entry at \mathbf{r}_μ such that $e_{\mathbf{r}_\mu}^T g_j = g_j(\mathbf{r}_\mu)$. Then

$$\chi_0 g_{\text{loc},j} \approx W \Pi^T g_{\text{loc},j} := \tilde{\chi}_0[\{g_{\text{loc},j}\}] g_{\text{loc},j}. \quad (2.29)$$

Note that the notation $\tilde{\chi}_0[\{g_{\text{loc},j}\}]$ emphasizes the dependence on the vectors that $\tilde{\chi}_0$ applies to. In other words, $\tilde{\chi}_0[\{g_{\text{loc},j}\}]$ is designed to only agree with χ_0 when applied to vectors $\{g_{\text{loc},j}\}$, and the difference between $\tilde{\chi}_0$ and χ_0 is not controlled in the space orthogonal to that spanned by these vectors. The rank of $\tilde{\chi}_0[\{g_{\text{loc},j}\}]$ is only N_μ , while the singular values of χ_0 have a much slower decay rate.

In the case when only local pseudopotential is used, the Dyson equation (2.15) is simplified as

$$u_j = \chi g_{\text{loc},j} = u_{0,j} + \chi_0 f_{\text{hxc}} u_j. \quad (2.30)$$

Here $u_{0,j} := \chi_0 g_{\text{loc},j}$ is called the non-self-consistent response, and has been computed using the algorithm described above.

In order to solve Eq. (2.30), we do not only need to evaluate $\chi_0 g_{\text{loc},j}$, but also the application of χ_0 to the self-consistent response $f_{\text{hxc}} u_j$ which is not known *a priori*. If we build a library of right hand side vectors so that the application of χ_0 remains accurate throughout the iteration process of solving Eq. (2.30), the computational complexity can quickly increase. Instead it is much more efficient to *adaptively compress* the polarizability operator χ_0 .

Note that for any given set of functions $\{u_j\}$, we can construct an operator $\tilde{\chi}_0[\{f_{\text{hxc}} u_j\}]$ so that $\tilde{\chi}_0$ agrees well with χ_0 when applied to the vectors $\{f_{\text{hxc}} u_j\}$. The Dyson equation can be rewritten as

$$u_j = (I - \tilde{\chi}_0[\{f_{\text{hxc}} u_j\}])^{-1} u_{0,j}. \quad (2.31)$$

Note that $\tilde{\chi}_0[\{f_{\text{hxc}}u_j\}]$ is a low rank operator, and the matrix inverse in Eq. (2.31) can be efficiently evaluated using the Sherman-Morrison-Woodbury formula.

Eq. (2.31) yields an iterative scheme

$$u^{k+1} = (I - \tilde{\chi}_0[\{f_{\text{hxc}}u^k\}])^{-1}u_0. \quad (2.32)$$

In the equation we omitted the j subindex of u . The convergence of the modified fixed point iteration (2.32) can be understood as follows. At the iteration step k , the scheme and the true solution respectively satisfy

$$\begin{aligned} u^{k+1} &= u_0 + \tilde{\chi}_0[\{f_{\text{hxc}}u^k\}]f_{\text{hxc}}u^{k+1}, \\ u^* &= u_0 + \chi_0f_{\text{hxc}}u^*. \end{aligned} \quad (2.33)$$

Let $e^k = u^k - u^*$ be the error at the iteration step k . We have

$$\begin{aligned} e^{k+1} &= \tilde{\chi}_0[\{f_{\text{hxc}}u^k\}]f_{\text{hxc}}u^{k+1} - \chi_0f_{\text{hxc}}u^* \\ &= \tilde{\chi}_0[\{f_{\text{hxc}}u^k\}]f_{\text{hxc}}u^{k+1} - \chi_0f_{\text{hxc}}u^{k+1} + \chi_0f_{\text{hxc}}u^{k+1} - \chi_0f_{\text{hxc}}u^* \\ &= \eta^k + \chi_0f_{\text{hxc}}e^{k+1}. \end{aligned} \quad (2.34)$$

Here

$$\eta^k := (\tilde{\chi}_0[\{f_{\text{hxc}}u^k\}] - \chi_0)f_{\text{hxc}}u^{k+1}, \quad (2.35)$$

which characterizes the discrepancy between $\tilde{\chi}_0$ and χ_0 when applied to the unknown vector $f_{\text{hxc}}u^{k+1}$. Therefore the error at the $(k+1)$ -th step satisfies

$$e^{k+1} = (I - \chi_0f_{\text{hxc}})^{-1}\eta^k. \quad (2.36)$$

Since χ_0 is negative semi-definite, the norm of $(I - \chi_0f_{\text{hxc}})^{-1}$ is bounded from above by one. Hence the error goes to zero if the error of compression η^k converges to 0.

To summarize, the ACP formulation has three key ingredients: Compress the right hand side; Disentangle the energy dependence; Adaptively compress the polarizability operator.

3. Split representation of the adaptively compressed polarizability operator. In this section, we demonstrate how to generalize the ACP formulation in section 2.3 for efficient phonon calculations of real materials. To this end we need to treat the nonlocal pseudopotential, as well as temperature effects especially for metallic systems. We demonstrate that the new split representation maintains the $\mathcal{O}(N_e^3)$ complexity, and improves all key steps in the ACP formulation, including Chebyshev interpolation of energy levels, iterative solution of Sternheimer equations, and convergence of the Dyson equations.

The split representation of the polarizability operator first chooses two cutoff energies $\varepsilon_{\tilde{N}_{\text{cut}}} > \varepsilon_{N_{\text{cut}}} \geq \mu$, and splits the right hand side of Eq. (2.18) into two terms

$$\begin{aligned}
\mathfrak{X}_0 \mathbf{g} \approx & \left[\left(\sum_{i=1}^{N_{\text{cut}}} \sum_{a=N_{\text{cut}}+1}^{\tilde{N}_{\text{cut}}} \frac{f_a - f_i}{\varepsilon_a - \varepsilon_i} \psi_a (\psi_a^* \mathbf{g} \psi_i) \psi_i^* + \text{h.c.} \right) \right. \\
& + \left. \sum_{i=1}^{N_{\text{cut}}} \sum_{a=1}^{N_{\text{cut}}} \frac{f_a - f_i}{\varepsilon_a - \varepsilon_i} \psi_a (\psi_a^* \mathbf{g} \psi_i) \psi_i^* \right] \\
& + \left[\sum_{i=1}^{N_{\text{cut}}} \sum_{a=\tilde{N}_{\text{cut}}+1}^{\infty} \frac{f_i}{\varepsilon_i - \varepsilon_a} \psi_a (\psi_a^* \mathbf{g} \psi_i) \psi_i^* + \text{h.c.} \right] \\
:= & \mathfrak{X}_0^{(s)} \mathbf{g} + \mathfrak{X}_0^{(r)} \mathbf{g}.
\end{aligned} \tag{3.1}$$

Here the first and second brackets split $\mathfrak{X}_0 \mathbf{g}$ into a singular component $\mathfrak{X}_0^{(s)} \mathbf{g}$ and a regular component $\mathfrak{X}_0^{(r)} \mathbf{g}$, respectively. The Hermitian conjugate appears for the same reason as in Eq. (2.20) when treating insulating systems. $\mathfrak{X}_0^{(s)}$ is called the singular component because for systems with small gaps, the ratio $(f_a - f_i)/(\varepsilon_a - \varepsilon_i)$ can be as large as $1/\varepsilon_g$. When the physical band gap ε_g is small, this term becomes numerically singular to treat in the iterative solution of Sternheimer equations as well as the Chebyshev interpolation. On the other hand, the term $f_i/(\varepsilon_i - \varepsilon_a)$ is bounded from above by $1/\tilde{\varepsilon}_g$, where $\tilde{\varepsilon}_g = \varepsilon_{\tilde{N}_{\text{cut}}+1} - \varepsilon_{N_{\text{cut}}}$ is called the *effective gap*. As the effective gap $\tilde{\varepsilon}_g$ increases, the magnitude of $\mathfrak{X}_0^{(r)}$ also decreases. In order to efficiently treat the singular part, we assume that the eigenfunctions $\{\psi_k\}_{k=1}^{\tilde{N}_{\text{cut}}}$ have been computed using an iterative eigensolver. The cost for obtaining the additional eigenvectors is modest, given that the ground state DFT calculation already prepares the eigenvectors $\{\psi_k\}_{k=1}^{N_{\text{cut}}}$.

The approximation in Eq. (3.1) only comes from that as ε increases above the chemical potential μ , the occupation number $f_i = \frac{1}{1+e^{\beta(\varepsilon_i - \mu)}}$ decays exponentially. Then we can choose $\varepsilon_{N_{\text{cut}}}$ large enough so that $f(\varepsilon_{N_{\text{cut}}+1})$ is sufficiently small and can be approximated by 0. For insulating systems we can simply choose $N_{\text{cut}} = N_e$. The second energy cutoff $\varepsilon_{\tilde{N}_{\text{cut}}}$ defines an effective gap $\tilde{\varepsilon}_g$, of which the role will be discussed later. The split representation requires the solution of eigenpairs (ε_i, ψ_i) of H for $i \leq \tilde{N}_{\text{cut}}$. Fig. 3.1 illustrates the position of the cutoff energies along the energy spectrum, with respect to the occupation number given by the Fermi-Dirac distribution.

3.1. Compression of the regular component of the polarizability operator. One advantage of the split representation is that in the regular component, the contribution from f_a vanishes, and hence $\mathfrak{X}_0^{(r)} \mathbf{g}$ can be evaluated using Sternheimer equations to eliminate the need of computing all the unoccupied orbitals as follows

$$\mathfrak{X}_0^{(r)} \mathbf{g} = \sum_{i=1}^{N_{\text{cut}}} f_i Q_c (\varepsilon_i - H)^{-1} Q_c (\mathbf{g} \psi_i) \psi_i^* + \text{h.c.} \tag{3.2}$$

Here the projection operator $Q_c = I - \sum_{i=1}^{\tilde{N}_{\text{cut}}} \psi_i \psi_i^*$ projects a vector to the space which is orthogonal to the space spanned by $\{\psi_i\}_{i=1}^{\tilde{N}_{\text{cut}}}$. When all order 2 tensors $\{\mathbf{g}_j\}$ are considered together, Eq. (3.2) requires the solution of

$$Q_c (\varepsilon_i - H) Q_c \zeta_{ij} = Q_c (\mathbf{g}_j \psi_i), \quad i = 1, \dots, N_{\text{cut}}, \quad j = 1, \dots, d \times N_A. \tag{3.3}$$

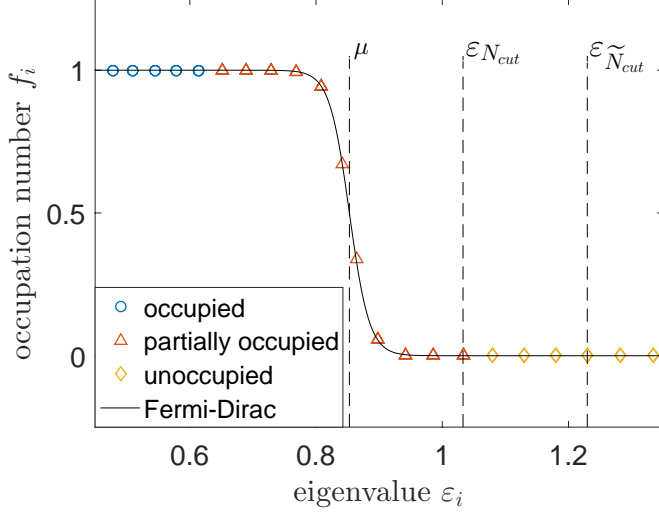


Fig. 3.1: Schematic illustration of the cutoff energies with respect to the Fermi-Dirac distribution.

Here each solution ζ_{ij} is still a vector. The adaptive compression of $\mathfrak{X}_0 \mathbf{g}_j$ then parallels the adaptive compression of $\chi_0 g_{loc,j}$ as in section 2.3, as detailed below.

The first step is to construct the collection of the right hand side vectors $M_{ij} = \mathbf{g}_j \psi_i$. Since the kernel of the nonlocal pseudopotential from each atom is compactly supported in the real space, the computational cost for generating M is in fact dominated by the cost associated with the local component $g_{loc,j}$. Hence the overall cost is still $\mathcal{O}(N_e^3)$. The interpolative separable density fitting procedure can then proceed as before, and generate a set of compressed vectors $\{\xi_\mu\}_{\mu=1}^{N_\mu}$ as well as the selected columns $\{\mathbf{r}_\mu\}_{\mu=1}^{N_\mu}$. The interpolation decomposition then reads

$$M_{ij}(\mathbf{r}) = (\mathbf{g}_j \psi_i)(\mathbf{r}) \approx \sum_{\mu} \xi_{\mu}(\mathbf{r})(\mathbf{g}_j \psi_i)(\mathbf{r}_{\mu}). \quad (3.4)$$

The second step is the disentanglement of the energy dependence. We choose the Chebyshev interpolation points on the interval $\mathcal{I} = [\varepsilon_1, \varepsilon_{N_{cut}}]$. Since the number of Chebyshev interpolation points is now controlled by the effective gap as $N_c \sim \mathcal{O}(\sqrt{\mathcal{I}/\tilde{\varepsilon}_g})$. Note that the gap ε_g (which can be small or zero) is now replaced by the effective gap $\tilde{\varepsilon}_g$. In practice we observe that it is often sufficient to choose N_c to be $5 \sim 10$.

With the Chebyshev interpolation procedure, the Sternheimer equation still takes the form (2.26), with Q replaced by Q_c . The operator $Q_c(\varepsilon_c - H)Q_c$ is a negative definite operator, with eigenvalue bounded from above by $-\tilde{\varepsilon}_g$. As the effective gap increases, the linear system associated with the Sternheimer equation also becomes better conditioned and the number of MINRES iterations can decrease. Typically we observe that MINRES can converge with around 10 steps.

After the solution of the Sternheimer equations, Eq. (3.2) becomes

$$\mathfrak{X}_0^{(r)} \mathfrak{g}_j \approx \sum_{i=1}^{N_{\text{cut}}} \sum_{\mu=1}^{N_\mu} f_i(\mathfrak{g}_j \psi_i)(\mathbf{r}_\mu) \left(\sum_{c=1}^{N_c} \tilde{\zeta}_{c\mu} \prod_{c' \neq c} \frac{\varepsilon_i - \tilde{\varepsilon}_{c'}}{\tilde{\varepsilon}_c - \tilde{\varepsilon}_{c'}} \right) \psi_i^* + \text{h.c.} \quad (3.5)$$

Since that \mathfrak{g}_j can be split into a local and a nonlocal component, we have

$$(\mathfrak{g}_j \psi_i)(\mathbf{r}_\mu) = g_{\text{loc},j}(\mathbf{r}_\mu) \psi_i(\mathbf{r}_\mu) + (\mathfrak{g}_{\text{nl},j} \psi_i)(\mathbf{r}_\mu). \quad (3.6)$$

Define

$$\mathfrak{W}_\mu^{(r)} = \sum_{i=1}^{N_{\text{cut}}} \left(\sum_{c=1}^{N_c} \tilde{\zeta}_{c\mu} \prod_{c' \neq c} \frac{\varepsilon_i - \tilde{\varepsilon}_{c'}}{\tilde{\varepsilon}_c - \tilde{\varepsilon}_{c'}} \right) \psi_i(\mathbf{r}_\mu) f_i \psi_i^* + \text{h.c.}, \quad (3.7)$$

and introduce the permutation matrix Π as in Eq. (2.29), then Eq. (3.5) becomes

$$\begin{aligned} \mathfrak{X}_0^{(r)} \mathfrak{g}_j \approx & \sum_{\mu=1}^{N_\mu} \mathfrak{W}_\mu^{(r)} (\Pi_\mu^T g_{\text{loc},j}) \\ & + \left[\sum_{i=1}^{N_{\text{cut}}} \sum_{\mu=1}^{N_\mu} f_i(\mathfrak{g}_{\text{nl},j} \psi_i)(\mathbf{r}_\mu) \left(\sum_{c=1}^{N_c} \tilde{\zeta}_{c\mu} \prod_{c' \neq c} \frac{\varepsilon_i - \tilde{\varepsilon}_{c'}}{\tilde{\varepsilon}_c - \tilde{\varepsilon}_{c'}} \right) \psi_i^* + \text{h.c.} \right] \end{aligned} \quad (3.8)$$

At first glance, Eq. (3.8) does not lead to any simplification compared to Eq. (3.5). However, since the nonlocal component of \mathfrak{g}_j is compactly supported, for each $\mathfrak{g}_{\text{nl},j}$ there are only $\mathcal{O}(1)$ number of points $\{\mathbf{r}_\mu\}$ that contributes to $(\mathfrak{g}_{\text{nl},j} \psi_i)(\mathbf{r}_\mu)$. Hence the last term in Eq. (3.8) is much easier to evaluate than the direct evaluation of Eq. (3.5).

3.2. Compression of the singular component of the polarizability operator. In practical calculations, numerical results indicate that it can be sufficient to choose $\tilde{N}_{\text{cut}} \leq 2N_e$, and hence the computation of $\mathfrak{X}_0^{(s)} \mathfrak{g}$ can even be directly evaluated according to Eq. (3.1). Compared to Eq. (2.18), the computation of $\mathfrak{X}_0^{(s)} \mathfrak{g}$ still scales as $\mathcal{O}(N_e^4)$, but the preconstant is much smaller. In this section we demonstrate that with a contour integral reformulation, we can compress the singular component as well with $\mathcal{O}(N_e^3)$ complexity.

According to the derivation in Appendix A, $\mathfrak{X}_0^{(s)} \mathfrak{g}$ can be evaluated using the contour integral formulation as

$$\begin{aligned} \mathfrak{X}_0^{(s)} \mathfrak{g} = & \left[\frac{1}{2\pi i} \oint_{\mathcal{C}} f(z) (z - H_{c,2})^{-1} \mathfrak{g} (z - H_{c,1})^{-1} dz + \text{h.c.} \right] \\ & + \frac{1}{2\pi i} \oint_{\mathcal{C}} f(z) (z - H_{c,1})^{-1} \mathfrak{g} (z - H_{c,1})^{-1} dz \end{aligned} \quad (3.9)$$

Here $H_{c,1} = \sum_{i=1}^{N_{\text{cut}}} \psi_i \varepsilon_i \psi_i^*$, $H_{c,2} = \sum_{i=N_{\text{cut}}+1}^{\tilde{N}_{\text{cut}}} \psi_i \varepsilon_i \psi_i^*$ are the Hamiltonian operators projected to the subspace spanned by the first N_{cut} states, and to the subspace spanned by the following $(\tilde{N}_{\text{cut}} - N_{\text{cut}})$ states, respectively. Before moving on to further discussion, we note that the numerically exact spectral decomposition of $H_{c,1}$ and $H_{c,2}$ is the key to reducing the complexity.

The contour integral in Eq. (3.9) can be discretized to obtain a numerical scheme. Let the integration nodes and weights be denoted by $\{z_p, \omega_p\}_{p=1}^{N_p}$, i.e.

$$\frac{1}{2\pi i} \oint_{\mathcal{C}} h(z) dz \approx \sum_{p=1}^{N_p} \omega_p h(z_p), \quad (3.10)$$

for suitable $h(z)$, and the discretization scheme can be obtained using rational approximation methods [25, 33, 32]. Then we have

$$\begin{aligned} \mathfrak{X}_0^{(s)} \mathfrak{g}_j &\approx \left[\sum_{p=1}^{N_p} \omega_p (z_p - H_{c,2})^{-1} \mathfrak{g}_j (z_p - H_{c,1})^{-1} + \text{h.c.} \right] \\ &\quad + \sum_{p=1}^{N_p} \omega_p (z_p - H_{c,1})^{-1} \mathfrak{g}_j (z_p - H_{c,1})^{-1} \\ &= \left[\sum_{p=1}^{N_p} \omega_p \sum_{i=1}^{N_{\text{cut}}} (z_p - H_{c,2})^{-1} (\mathfrak{g}_j \psi_i) (z_p - \varepsilon_i)^{-1} \psi_i^* + \text{h.c.} \right] \\ &\quad + \sum_{p=1}^{N_p} \omega_p \sum_{i=1}^{N_{\text{cut}}} (z_p - H_{c,1})^{-1} (\mathfrak{g}_j \psi_i) (z_p - \varepsilon_i)^{-1} \psi_i^*, \end{aligned} \quad (3.11)$$

where the equality is derived from the spectral decompositions of $H_{c,1}, H_{c,2}$. When all $\{\mathfrak{g}_j\}$ are considered together, we use again the interpolative separable density fitting (3.4) and obtain

$$\begin{aligned} \mathfrak{X}_0^{(s)} \mathfrak{g}_j &\approx \left[\sum_{p=1}^{N_p} \omega_p \sum_{i=1}^{N_{\text{cut}}} (z_p - H_{c,2})^{-1} \sum_{\mu=1}^{N_{\mu}} \xi_{\mu}(\mathfrak{g}_j \psi_i)(\mathbf{r}_{\mu}) (z_p - \varepsilon_i)^{-1} \psi_i^* + \text{h.c.} \right] \\ &\quad + \sum_{p=1}^{N_p} \omega_p \sum_{i=1}^{N_{\text{cut}}} (z_p - H_{c,1})^{-1} \sum_{\mu=1}^{N_{\mu}} \xi_{\mu}(\mathfrak{g}_j \psi_i)(\mathbf{r}_{\mu}) (z_p - \varepsilon_i)^{-1} \psi_i^* \\ &= \left[\sum_{i=1}^{N_{\text{cut}}} \sum_{\mu=1}^{N_{\mu}} (\mathfrak{g}_j \psi_i)(\mathbf{r}_{\mu}) \left(\sum_{p=1}^{N_p} \tilde{\zeta}_{2,p\mu}^{(s)} \omega_p (z_p - \varepsilon_i)^{-1} \right) \psi_i^* + \text{h.c.} \right] \\ &\quad + \sum_{i=1}^{N_{\text{cut}}} \sum_{\mu=1}^{N_{\mu}} (\mathfrak{g}_j \psi_i)(\mathbf{r}_{\mu}) \left(\sum_{p=1}^{N_p} \tilde{\zeta}_{1,p\mu}^{(s)} \omega_p (z_p - \varepsilon_i)^{-1} \right) \psi_i^*. \end{aligned} \quad (3.12)$$

In the last equation of (3.12), we have defined the solution $\tilde{\zeta}_{\theta,p\mu}^{(s)} := (z_p - H_{c,\theta})^{-1} \xi_{\mu}$, $\theta = 1, 2$, which can be numerically exactly computed from the spectral decompositions of $H_{c,1}, H_{c,2}$ respectively. We use the same strategy as in Eq. (3.8) to handle the contribution from $(\mathfrak{g}_j \psi_i)(\mathbf{r}_{\mu})$. Define

$$\begin{aligned} \mathfrak{W}_{\mu}^{(s)} &= \left[\sum_{i=1}^{N_{\text{cut}}} \psi_i(\mathbf{r}_{\mu}) \left(\sum_{p=1}^{N_p} \tilde{\zeta}_{2,p\mu}^{(s)} \omega_p (z_p - \varepsilon_i)^{-1} \right) \psi_i^* + \text{h.c.} \right] \\ &\quad + \sum_{i=1}^{N_{\text{cut}}} \psi_i(\mathbf{r}_{\mu}) \left(\sum_{p=1}^{N_p} \tilde{\zeta}_{1,p\mu}^{(s)} \omega_p (z_p - \varepsilon_i)^{-1} \right) \psi_i^*, \end{aligned} \quad (3.13)$$

and use the same permutation matrix Π as in Eq. (2.29), then Eq. (3.12) becomes

$$\begin{aligned} \mathfrak{X}_0^{(s)} \mathfrak{g}_j &\approx \sum_{\mu=1}^{N_\mu} \mathfrak{W}_\mu^{(s)} (\Pi_\mu^T g_{\text{loc},j}) \\ &+ \left[\sum_{i=1}^{N_{\text{cut}}} \sum_{\mu=1}^{N_\mu} (\mathfrak{g}_{\text{nl},j} \psi_i)(\mathbf{r}_\mu) \left(\sum_{p=1}^{N_p} \tilde{\zeta}_{2,p\mu}^{(s)} \omega_p (z_p - \varepsilon_i)^{-1} \right) \psi_i^* + \text{h.c.} \right] \\ &+ \sum_{i=1}^{N_{\text{cut}}} \sum_{\mu=1}^{N_\mu} (\mathfrak{g}_{\text{nl},j} \psi_i)(\mathbf{r}_\mu) \left(\sum_{p=1}^{N_p} \tilde{\zeta}_{1,p\mu}^{(s)} \omega_p (z_p - \varepsilon_i)^{-1} \right) \psi_i^*. \end{aligned} \quad (3.14)$$

3.3. Adaptive compression for solving the Dyson equation. Recall the Dyson equation (2.15), and so far we have computed the non-self-consistent response $\mathbf{u}_{0,j} := \mathfrak{X}_0 \mathfrak{g}_j$ using the split representation. In order to solve the Dyson equation, we still need to evaluate $\mathfrak{X}_0 \mathfrak{f}_{\text{hxc}} \mathbf{u}$ self-consistently. Use the locality structure of $\mathfrak{f}_{\text{hxc}}$ as in Eq. (2.16), we have

$$(\mathfrak{X}_0 \mathfrak{f}_{\text{hxc}} \mathbf{u})(\mathbf{r}, \mathbf{r}') = \int \mathfrak{X}_0(\mathbf{r}, \mathbf{r}'; \mathbf{r}'', \mathbf{r}'') f_{\text{hxc}}(\mathbf{r}'', \mathbf{r}''') \mathbf{u}(\mathbf{r}''', \mathbf{r}''') d\mathbf{r}'' d\mathbf{r}'''. \quad (3.15)$$

It is important to observe that Eq. (3.15) only requires the *diagonal elements* of \mathbf{u} . Hence the self-consistent solution of the Dyson equation (2.15) only requires a set of equations for these diagonal elements:

$$\mathbf{u}_j(\mathbf{r}, \mathbf{r}) = \mathbf{u}_{0,j}(\mathbf{r}, \mathbf{r}) + \int \mathfrak{X}_0(\mathbf{r}, \mathbf{r}; \mathbf{r}'', \mathbf{r}'') f_{\text{hxc}}(\mathbf{r}'', \mathbf{r}''') \mathbf{u}(\mathbf{r}''', \mathbf{r}''') d\mathbf{r}'' d\mathbf{r}'''. \quad (3.16)$$

Define $u_j(\mathbf{r}) = \mathbf{u}_j(\mathbf{r}, \mathbf{r})$ and $u_{0,j}(\mathbf{r}) = \mathbf{u}_{0,j}(\mathbf{r}, \mathbf{r})$ and use the linear algebra notation, then Eq. (3.16) becomes a reduced Dyson equation

$$u_j = u_{0,j} + \chi_0 f_{\text{hxc}} u_j. \quad (3.17)$$

Note that Eq. (3.17) becomes precisely the same as Eq. (2.30), which does not involve nonlocal pseudopotentials. However, the important difference is that in Eq. (3.17), $u_{0,j}$ is taken from the diagonal elements of $\mathbf{u}_{0,j}$, which properly takes into account the nonlocal pseudopotential both in the Hamiltonian and in the non-self-consistent response.

Before moving on to the discussion of solving the reduced Dyson equation, we write out the explicit format of the diagonal part $u_{0,j} = \mathbf{u}_{0,j}$. Define $W_\mu^{(r)}(\mathbf{r}) = \mathfrak{W}_\mu^{(r)}(\mathbf{r}, \mathbf{r})$, $W_\mu^{(s)}(\mathbf{r}) = \mathfrak{W}_\mu^{(s)}(\mathbf{r}, \mathbf{r})$, the diagonal part of Eq. (3.8) reads

$$\begin{aligned} \left(\mathfrak{X}_0^{(r)} \mathfrak{g}_j \right) (\mathbf{r}, \mathbf{r}) &\approx \sum_{\mu=1}^{N_\mu} W_\mu^{(r)}(\mathbf{r}) (\Pi_\mu^T g_{\text{loc},j}) \\ &+ \left[\sum_{i=1}^{N_{\text{cut}}} \sum_{\mu=1}^{N_\mu} f_i(\mathfrak{g}_{\text{nl},j} \psi_i)(\mathbf{r}_\mu) \left(\sum_{c=1}^{N_c} \tilde{\zeta}_{c\mu}(\mathbf{r}) \prod_{c' \neq c} \frac{\varepsilon_i - \tilde{\varepsilon}_{c'}}{\tilde{\varepsilon}_c - \tilde{\varepsilon}_{c'}} \right) \psi_i^*(\mathbf{r}) + \text{h.c.} \right]. \end{aligned} \quad (3.18)$$

The diagonal part of Eq. (3.14) reads

$$\begin{aligned}
\left(\mathfrak{X}_0^{(s)} \mathfrak{g}_j\right)(\mathbf{r}, \mathbf{r}) &\approx \sum_{\mu=1}^{N_\mu} W_\mu^{(s)}(\mathbf{r}) (\Pi_\mu^T g_{\text{loc},j}) \\
&+ \left[\sum_{i=1}^{N_{\text{cut}}} \sum_{\mu=1}^{N_\mu} (\mathfrak{g}_{\text{nl},j} \psi_i)(\mathbf{r}_\mu) \left(\sum_{p=1}^{N_p} \tilde{\zeta}_{2,p\mu}^{(s)}(\mathbf{r}) \omega_p(z_p - \varepsilon_i)^{-1} \right) \psi_i^*(\mathbf{r}) + \text{h.c.} \right] \\
&+ \sum_{i=1}^{N_{\text{cut}}} \sum_{\mu=1}^{N_\mu} (\mathfrak{g}_{\text{nl},j} \psi_i)(\mathbf{r}_\mu) \left(\sum_{p=1}^{N_p} \tilde{\zeta}_{1,p\mu}^{(s)}(\mathbf{r}) \omega_p(z_p - \varepsilon_i)^{-1} \right) \psi_i^*(\mathbf{r}).
\end{aligned} \tag{3.19}$$

The reduced Dyson equation (3.17) can be readily solved using the same adaptive compression strategy in section 2.3. More specifically, we can replace \mathfrak{g}_j by the local potential $\text{diag}[f_{\text{hxc}} u_j]$, and only take the diagonal elements in Eq. (3.8) and (3.14) to obtain $\chi_0 f_{\text{hxc}} u_j$. Moreover, since both the regular part $\chi_0^{(r)}$ and the singular part $\chi_0^{(s)}$ preserve a low-rank nature, Sherman-Morrison-Woodbury formula can still be used in the fixed point iteration. The separated treatment of the singular and regular parts reduces the error of the compressed χ_0 as in Eq. (2.35). Therefore it also accelerates the convergence of the Dyson equation. The complete iteration process to solve the Dyson equations is defined in Alg. 1.

Algorithm 1: Computing $U := [u_j]$ with the split representation of adaptively compressed polarizability operator.

Input:

$\{\mathfrak{g}_j\}$. Stopping criterion δ .

Eigenpairs corresponding to occupied orbitals $\{\psi_i, \varepsilon_i\}, i = 1, \dots, \tilde{N}_{\text{cut}}$

Output: $U \approx \chi G$

1. Compute $U_0 := [u_{0,j}]$ using Eq. (3.8) and (3.14) (only the diagonal elements).

2. **Do**

(a) Replace $\{\mathfrak{g}_j\}$ with $\text{diag}[f_{\text{hxc}} u_j^k]$ to obtain $W^{(r)k}$ and $W^{(s)k}$ and Π^k in Eq. (3.7) and (3.13). Define $W^k = W^{(s)k} + W^{(r)k}$.

(b) Update U^{k+1} using Sherman-Morrison-Woodbury formula

$$\begin{aligned}
U^{k+1} &= \left(I - W^k (\Pi^k)^T f_{\text{hxc}} \right)^{-1} U_0 \\
&= U_0 + W^k \left(I - (\Pi^k)^T f_{\text{hxc}} W^k \right)^{-1} (\Pi^k)^T f_{\text{hxc}} U_0
\end{aligned}$$

(c) $k \leftarrow k + 1$

until $\frac{\|U^k - U^{k-1}\|}{\|U^{k-1}\|} < \delta$ or maximum number of iterations is reached.

Once the self-consistent $\mathbf{u}_j(\mathbf{r}, \mathbf{r})$ are obtained, one can formally reconstruct $\mathbf{u}(\mathbf{r}, \mathbf{r}')$ by using the split representation again in Eq. (3.8) and (3.14). Finally \mathbf{u}_j will be integrated with $\mathfrak{g}_{j'}$ as in Eq. (2.11) to compute the Hessian matrix for phonon calculations, which will be further discussed in detail in the next section.

3.4. Phonon Calculation. For the purpose of phonon calculation, \mathbf{u}_j (representing a component of $\frac{\partial P}{\partial \mathbf{R}_I}$) will be integrated with $\mathfrak{g}_{j'}$ (representing a component of

$\frac{\partial V_{\text{ion}}}{\partial \mathbf{R}_J}$) as in Eq. (2.11) to compute the Hessian matrix for phonon calculations. The integration with local components can be readily computed once the self-consistent response $u_j(\mathbf{r})$ is obtained by solving the reduced Dyson equation. The integration with nonlocal components $\mathbf{g}_{\text{nl},j}$ would require the construction of $\mathbf{u}(\mathbf{r}, \mathbf{r}')$. However since $\mathbf{g}_{\text{nl},j}$ is compactly supported, one could avoid the full construction of $\mathbf{u}(\mathbf{r}, \mathbf{r}')$ by embedding the integration process into the construction of $\mathbf{u}(\mathbf{r}, \mathbf{r}')$. This is important for maintaining the reduced scaling of the algorithm.

In this section, we show the construction of integral in Eq. (2.12). For simplicity, the indexes I, J are ignored. Starting from the Dyson equation,

$$\mathbf{u}(\mathbf{r}, \mathbf{r}') = (\mathfrak{X}_0 \mathbf{g})(\mathbf{r}, \mathbf{r}') + (\mathfrak{X}_0 \mathfrak{f}_{\text{hxc}} \mathbf{u})(\mathbf{r}, \mathbf{r}'), \quad (3.20)$$

an element of the Hessian matrix requires calculation of

$$\int \mathbf{g}(\mathbf{r}, \mathbf{r}') \mathbf{u}(\mathbf{r}, \mathbf{r}') \, d\mathbf{r} \, d\mathbf{r}' = \int [\mathbf{g}(\mathbf{r}, \mathbf{r}') (\mathfrak{X}_0 \mathbf{g})(\mathbf{r}, \mathbf{r}') + \mathbf{g}(\mathbf{r}, \mathbf{r}') (\mathfrak{X}_0 \mathfrak{f}_{\text{hxc}} \mathbf{u})(\mathbf{r}, \mathbf{r}')] \, d\mathbf{r} \, d\mathbf{r}'. \quad (3.21)$$

Recall that $\mathbf{g}(\mathbf{r}, \mathbf{r}') = g_{\text{loc}}(\mathbf{r}) \delta(\mathbf{r}' - \mathbf{r}) + \mathbf{g}_{\text{nl}}(\mathbf{r}, \mathbf{r}')$, the integral for the local part of can be easily calculated (letting $u(\mathbf{r}) = \mathbf{u}(\mathbf{r}, \mathbf{r})$)

$$\int g_{\text{loc}}(\mathbf{r}, \mathbf{r}') \mathbf{u}(\mathbf{r}, \mathbf{r}') \, d\mathbf{r} \, d\mathbf{r}' = \int g_{\text{loc}}(\mathbf{r}) u(\mathbf{r}) \, d\mathbf{r}. \quad (3.22)$$

For the non-local potential, using Eq. (3.8) and Eq. (3.14), we have

$$\int \mathbf{g}_{\text{nl}}(\mathbf{r}, \mathbf{r}') \mathbf{u}(\mathbf{r}, \mathbf{r}') \, d\mathbf{r} \, d\mathbf{r}' = \int \mathbf{g}_{\text{nl}}(\mathbf{r}, \mathbf{r}') [(\mathfrak{X}_0 \mathbf{g})(\mathbf{r}, \mathbf{r}') + (\mathfrak{X}_0 \mathfrak{f}_{\text{hxc}} \mathbf{u})(\mathbf{r}, \mathbf{r}')] \, d\mathbf{r} \, d\mathbf{r}'. \quad (3.23)$$

Recall that $(\mathfrak{f}_{\text{hxc}} \mathbf{u})(\mathbf{r}, \mathbf{r}') = \delta(\mathbf{r} - \mathbf{r}') \int \mathfrak{f}_{\text{hxc}}(\mathbf{r}, \mathbf{r}'') u(\mathbf{r}'') \, d\mathbf{r}''$. So $(\mathfrak{f}_{\text{hxc}} \mathbf{u})(\mathbf{r}, \mathbf{r}')$ behaves as a local potential g_{loc} when applying \mathfrak{X}_0 to it. So the integral in Eq. (3.23) breaks down to four parts:

$$\begin{aligned} & \int \mathbf{g}_{\text{nl}}(\mathbf{r}, \mathbf{r}') (\mathfrak{X}_0^{(r)} \mathbf{g})(\mathbf{r}, \mathbf{r}') \, d\mathbf{r} \, d\mathbf{r}' \\ &= \int - \sum_{l=1}^L \gamma_l (b_l(\mathbf{r}) db_l^*(\mathbf{r}') + db_l(\mathbf{r}) b_l^*(\mathbf{r}')) (\mathfrak{X}_0^{(r)} \mathbf{g})(\mathbf{r}, \mathbf{r}') \, d\mathbf{r} \, d\mathbf{r}' \\ &= - \int d\mathbf{r} \, d\mathbf{r}' \sum_{l=1}^L \gamma_l (b_l(\mathbf{r}) db_l^*(\mathbf{r}') + db_l(\mathbf{r}) b_l^*(\mathbf{r}')) \sum_{\mu=1}^{N_\mu} \mathfrak{W}_\mu^{(r)}[\mathbf{g}](\mathbf{r}, \mathbf{r}') (\Pi_\mu[\mathbf{g}]^T g_{\text{loc}}) \\ &+ \left[- \sum_{l=1}^L \gamma_l \sum_{i=1}^{N_{\text{cut}}} \sum_{\mu=1}^{N_\mu} f_i(\mathbf{g}_{\text{nl}} \psi_i)(\mathbf{r}_\mu) \left(\sum_{c=1}^{N_c} \int d\mathbf{r} \tilde{\zeta}_{c\mu}(\mathbf{r}) b_l(\mathbf{r}) \prod_{c' \neq c} \frac{\varepsilon_i - \tilde{\varepsilon}_{c'}}{\tilde{\varepsilon}_c - \tilde{\varepsilon}_{c'}} \right) \int d\mathbf{r} \psi_i^*(\mathbf{r}') db_l^*(\mathbf{r}') \right. \\ &\quad \left. - \sum_{l=1}^L \gamma_l \sum_{i=1}^{N_{\text{cut}}} \sum_{\mu=1}^{N_\mu} f_i(\mathbf{g}_{\text{nl}} \psi_i)(\mathbf{r}_\mu) \left(\sum_{c=1}^{N_c} \int d\mathbf{r} \tilde{\zeta}_{c\mu}(\mathbf{r}) db_l(\mathbf{r}) \prod_{c' \neq c} \frac{\varepsilon_i - \tilde{\varepsilon}_{c'}}{\tilde{\varepsilon}_c - \tilde{\varepsilon}_{c'}} \right) \int d\mathbf{r} \psi_i^*(\mathbf{r}') b_l^*(\mathbf{r}') \right] \\ &+ \text{h.c. of previous bracket} \end{aligned} \quad (3.24)$$

$$\begin{aligned}
& \int \mathbf{g}_{\text{nl}}(\mathbf{r}, \mathbf{r}') (\mathfrak{X}_0^{(s)} \mathbf{g})(\mathbf{r}, \mathbf{r}') \, \mathbf{d}\mathbf{r} \, \mathbf{d}\mathbf{r}' \\
&= \int - \sum_{l=1}^L \gamma_l (b_l(\mathbf{r}) \, \text{d}b_l^*(\mathbf{r}') + \text{d}b_l(\mathbf{r}) b_l^*(\mathbf{r}')) (\mathfrak{X}_0^{(s)} \mathbf{g})(\mathbf{r}, \mathbf{r}') \, \mathbf{d}\mathbf{r} \, \mathbf{d}\mathbf{r}' \\
&= - \int \mathbf{d}\mathbf{r} \, \mathbf{d}\mathbf{r}' \sum_{l=1}^L \gamma_l (b_l(\mathbf{r}) \, \text{d}b_l^*(\mathbf{r}') + \text{d}b_l(\mathbf{r}) b_l^*(\mathbf{r}')) \sum_{\mu=1}^{N_\mu} \mathfrak{W}_\mu^{(s)}[\mathbf{g}](\mathbf{r}, \mathbf{r}') (\Pi_\mu[\mathbf{g}]^T g_{\text{loc}}) \\
&\quad + \left[- \sum_{l=1}^L \gamma_l \sum_{i=1}^{N_{\text{cut}}} \sum_{\mu=1}^{N_\mu} (\mathbf{g}_{\text{nl},j} \psi_i)(\mathbf{r}_\mu) \left(\sum_{p=1}^{N_p} \int \mathbf{d}\mathbf{r} \tilde{\zeta}_{2,p\mu}^{(s)}(\mathbf{r}) b_l(\mathbf{r}) \omega_p(z_p - \varepsilon_i)^{-1} \right) \int \mathbf{d}\mathbf{r}' \psi_i^*(\mathbf{r}') \, \text{d}b_l^*(\mathbf{r}') \right. \\
&\quad \left. - \sum_{l=1}^L \gamma_l \sum_{i=1}^{N_{\text{cut}}} \sum_{\mu=1}^{N_\mu} (\mathbf{g}_{\text{nl},j} \psi_i)(\mathbf{r}_\mu) \left(\sum_{p=1}^{N_p} \int \mathbf{d}\mathbf{r} \tilde{\zeta}_{2,p\mu}^{(s)}(\mathbf{r}) \, \text{d}b_l(\mathbf{r}) \omega_p(z_p - \varepsilon_i)^{-1} \right) \int \mathbf{d}\mathbf{r}' \psi_i^*(\mathbf{r}') b_l^*(\mathbf{r}') \right] \\
&\quad + \text{h.c. of previous bracket} \\
&\quad - \sum_{l=1}^L \gamma_l \sum_{i=1}^{N_{\text{cut}}} \sum_{\mu=1}^{N_\mu} (\mathbf{g}_{\text{nl},j} \psi_i)(\mathbf{r}_\mu) \left(\sum_{p=1}^{N_p} \int \mathbf{d}\mathbf{r} \tilde{\zeta}_{1,p\mu}^{(s)}(\mathbf{r}) b_l(\mathbf{r}) \omega_p(z_p - \varepsilon_i)^{-1} \right) \int \mathbf{d}\mathbf{r}' \psi_i^*(\mathbf{r}') \, \text{d}b_l^*(\mathbf{r}') \\
&\quad - \sum_{l=1}^L \gamma_l \sum_{i=1}^{N_{\text{cut}}} \sum_{\mu=1}^{N_\mu} (\mathbf{g}_{\text{nl},j} \psi_i)(\mathbf{r}_\mu) \left(\sum_{p=1}^{N_p} \int \mathbf{d}\mathbf{r} \tilde{\zeta}_{1,p\mu}^{(s)}(\mathbf{r}) \, \text{d}b_l(\mathbf{r}) \omega_p(z_p - \varepsilon_i)^{-1} \right) \int \mathbf{d}\mathbf{r}' \psi_i^*(\mathbf{r}') b_l^*(\mathbf{r}') \\
\end{aligned} \tag{3.25}$$

$$\begin{aligned}
& \int \mathbf{g}_{\text{nl}}(\mathbf{r}, \mathbf{r}') (\mathfrak{X}_0^{(r)} \mathbf{f}_{\text{hxc}} \mathbf{u})(\mathbf{r}, \mathbf{r}') \, \mathbf{d}\mathbf{r} \, \mathbf{d}\mathbf{r}' \\
&= \int - \sum_{l=1}^L \gamma_l (b_l(\mathbf{r}) \, \text{d}b_l^*(\mathbf{r}') + \text{d}b_l(\mathbf{r}) b_l^*(\mathbf{r}')) (\mathfrak{X}_0^{(r)} \mathbf{f}_{\text{hxc}} \mathbf{u})(\mathbf{r}, \mathbf{r}') \, \mathbf{d}\mathbf{r} \, \mathbf{d}\mathbf{r}' \\
&= - \int \mathbf{d}\mathbf{r} \, \mathbf{d}\mathbf{r}' \sum_{l=1}^L \gamma_l (b_l(\mathbf{r}) \, \text{d}b_l^*(\mathbf{r}') + \text{d}b_l(\mathbf{r}) b_l^*(\mathbf{r}')) \sum_{\mu=1}^{N_\mu} \mathfrak{W}_\mu^{(r)}[\mathbf{f}_{\text{hxc}} \mathbf{u}](\mathbf{r}, \mathbf{r}') (\Pi_\mu[\mathbf{f}_{\text{hxc}} \mathbf{u}]^T \mathbf{f}_{\text{hxc}} \mathbf{u}) \\
\end{aligned} \tag{3.26}$$

$$\begin{aligned}
& \int \mathbf{g}_{\text{nl}}(\mathbf{r}, \mathbf{r}') (\mathfrak{X}_0^{(s)} \mathbf{f}_{\text{hxc}} \mathbf{u})(\mathbf{r}, \mathbf{r}') \, \mathbf{d}\mathbf{r} \, \mathbf{d}\mathbf{r}' \\
&= \int - \sum_{l=1}^L \gamma_l (b_l(\mathbf{r}) \, \text{d}b_l^*(\mathbf{r}') + \text{d}b_l(\mathbf{r}) b_l^*(\mathbf{r}')) (\mathfrak{X}_0^{(s)} \mathbf{f}_{\text{hxc}} \mathbf{u})(\mathbf{r}, \mathbf{r}') \, \mathbf{d}\mathbf{r} \, \mathbf{d}\mathbf{r}' \\
&= - \int \mathbf{d}\mathbf{r} \, \mathbf{d}\mathbf{r}' \sum_{l=1}^L \gamma_l (b_l(\mathbf{r}) \, \text{d}b_l^*(\mathbf{r}') + \text{d}b_l(\mathbf{r}) b_l^*(\mathbf{r}')) \sum_{\mu=1}^{N_\mu} \mathfrak{W}_\mu^{(s)}[\mathbf{f}_{\text{hxc}} \mathbf{u}](\mathbf{r}, \mathbf{r}') (\Pi_\mu[\mathbf{f}_{\text{hxc}} \mathbf{u}]^T \mathbf{f}_{\text{hxc}} \mathbf{u}) \\
\end{aligned} \tag{3.27}$$

We remark that the \mathfrak{W} quantity depends on the tensors to which \mathfrak{X}_0 is applied. Note that in Eqs. (3.24), (3.25), (3.26), (3.27), terms like $\int \mathbf{d}\mathbf{r}' \psi_i^*(\mathbf{r}') b_l^*(\mathbf{r}')$ appear many

times, hence computing and storing them is necessary. Also one important fact is that $\mathbf{g}_{\text{nl},j}\psi_i(\mathbf{r}_\mu)$ is only non-zero for several \mathbf{r}_μ . This would result in a “fake” summation of N_μ , which is essential in reducing the complexity. Computation of Eq. (3.24) and Eq. (3.25) is only $\mathcal{O}(N_e)$. The complexity is discussed in detail in the following section.

3.5. Complexity. In this section we analyze the complexity of phonon calculation using the split representation of ACP formulation, especially those related to nonlocal pseudopotential.

The first part of the algorithm is to compute the diagonal elements $u_{0,j}$ in Eq. (3.18) and (3.19). For the local pseudopotential, the cost of constructing $W^{(r)}$ and $W^{(s)}$ is $\mathcal{O}(N_\mu N_{\text{cut}} N_c N_g) \sim \mathcal{O}(N_e^3)$ and $\mathcal{O}(N_\mu N_{\text{cut}} N_p N_g) \sim \mathcal{O}(N_e^3)$ respectively, since $N_\mu, N_{\text{cut}}, N_g \sim \mathcal{O}(N_e)$, and $N_c, N_p \sim \mathcal{O}(1)$. Note that the construction of $W^{(r)}, W^{(s)}$ does not depend on the index j , hence there is no factor of dN_A involved. For the nonlocal pseudopotential, as is discussed in Section 3.1, each nonlocal component of \mathbf{g}_j is compactly supported in the real space. Denote N_b as the grid points for the support of $\mathbf{g}_{\text{nl},j}$. Hence for each $\mathbf{g}_{\text{nl},j}$ there are only $N_b \sim \mathcal{O}(1)$ number of points \mathbf{r}_μ that contributes to $(\mathbf{g}_{\text{nl},j}\psi_i)(\mathbf{r}_\mu)$. So the cost associated with the nonlocal contribution is $\mathcal{O}(dN_A N_{\text{cut}} N_b N_c N_g) \sim \mathcal{O}(N_e^3)$ in Eq. (3.8) and $\mathcal{O}(dN_A N_{\text{cut}} N_b N_p N_g) \sim \mathcal{O}(N_e^3)$ in Eq. (3.14). Note that the dN_A factor comes from the fact that $\mathbf{g}_{\text{nl},j}\psi_i(\mathbf{r}_\mu)$ depends on index $j = 1, 2, \dots, dN_A$.

In every iteration step when solving the reduced Dyson equation, the complexity of the construction of W^k still cost $\mathcal{O}(N_e^3)$, as we just replaced \mathbf{g}_j by $\text{diag}[f_{\text{hxc}} u_j^k]$. Using Sherman-Morrison-Woodbury formula, the update of U^{k+1} cost $\mathcal{O}(N_g N_\mu dN_A + N_\mu^3 + N_\mu^2 dN_A) \sim \mathcal{O}(N_e^3)$. In practice, we observe we observe that the number of iterations does not increase with respect to the system size. To summarize, we know that the computation of $u_j(\mathbf{r})$ cost $\mathcal{O}(N_e^3)$ in total.

In order to assemble the information stored in \mathbf{u}_j to obtain the dynamical matrix for phonon calculations, \mathbf{u}_j will be integrated with $\mathbf{g}_{j'}$ as in Eq. (2.11). Before we move on to further discussion, we note that $\mathbf{u}_j(\mathbf{r}, \mathbf{r}'), \mathfrak{W}_\mu(\mathbf{r}, \mathbf{r}')$ are never constructed or stored. They are only stored in its factorized format. The integration with local components can be readily computed once the self-consistent response $u_j(\mathbf{r})$ is obtained by solving the reduced Dyson equation. The corresponding cost is $\mathcal{O}(d^2 N_A^2 N_g)$. The integration with nonlocal components $\mathbf{g}_{\text{nl},j}$ would require certain off-diagonal entries $\mathbf{u}(\mathbf{r}, \mathbf{r}')$. However since $\mathbf{g}_{\text{nl},j}$ is compactly supported, one could avoid the full construction of $\mathbf{u}(\mathbf{r}, \mathbf{r}')$ by embedding the integration process into the construction of $\mathbf{u}(\mathbf{r}, \mathbf{r}')$. As shown in Eqs. (3.24) and (3.25), the complexity for this integration is $\mathcal{O}(d^2 N_a^2 N_b N_{\text{cut}} N_c + 2d^2 N_a^2 N_{\text{cut}} N_b N_c) \sim \mathcal{O}(N_e^3)$ and $\mathcal{O}(d^2 N_a^2 N_b^2 N_{\text{cut}} N_p + 2d^2 N_a^2 N_{\text{cut}} N_b N_p) \sim \mathcal{O}(N_e^3)$, respectively. As for Eqs. (3.26) and (3.27), the complexity is $\mathcal{O}(d^2 N_a^2 N_b N_{\text{cut}} N_c) \sim \mathcal{O}(N_e^3)$ and $\mathcal{O}(d^2 N_a^2 N_b N_{\text{cut}} N_p) \sim \mathcal{O}(N_e^3)$, respectively. Diagonalizing the Hessian matrix costs $\mathcal{O}(N_a^3)$. In summary, the complexity of phonon calculation scales as $\mathcal{O}(N_e^3)$. This is further confirmed by numerical examples in 1D in the following section. Table 3.1 summarizes the complexity of all computation steps of split ACP.

4. Numerical examples. In this section, we demonstrate the performance of split ACP and compare it with DFPT and finite difference (FD) through two examples. The first example consists of a 1D reduced Hartree-Fock model problem that can be tuned to resemble a metallic system. The second one is a 3D aluminum cluster calculation performed using KSSOLV [48], which is a MATLAB toolbox for solving Kohn-Sham equations for small molecules and solids in three-dimensions. KSSOLV

Step	Equation	Complexity
Interpolation decomposition	Eq. (3.4)	$\mathcal{O}(N_g d N_A N_{\text{cut}})$ $+\mathcal{O}(N_g N_{\text{cut}} N_\mu)$
Diagonal element construction regular part	Eq. (3.18)	$\mathcal{O}(N_\mu N_{\text{cut}} N_c N_g)$ $+\mathcal{O}(d N_A N_{\text{cut}} N_b N_c N_g)$
Diagonal element construction Singular part	Eq. (3.19)	$\mathcal{O}(N_\mu N_{\text{cut}} N_p N_g)$ $+\mathcal{O}(d N_A N_{\text{cut}} N_b N_p N_g)$
The Dyson equation update	Step 2.(b) in Alg. 1	$\mathcal{O}(N_g N_\mu d N_A)$ $+\mathcal{O}(N_\mu^3 + N_\mu^2 d N_A)$
Reconstruction local potential	Eq. (3.22)	$\mathcal{O}(d^2 N_A^2 N_g)$
Reconstruction nonlocal pseudopotential	Eq. (3.24)	$\mathcal{O}(d^2 N_a^2 N_b N_{\text{cut}} N_c + 2d^2 N_a^2 N_{\text{cut}} N_b N_c)$
	Eq. (3.25)	$\mathcal{O}(d^2 N_a^2 N_b N_{\text{cut}} N_p + 2d^2 N_a^2 N_{\text{cut}} N_b N_p)$
	Eq. (3.26)	$\mathcal{O}(d^2 N_a^2 N_b N_{\text{cut}} N_c)$
	Eq. (3.27)	$\mathcal{O}(d^2 N_a^2 N_b N_{\text{cut}} N_p)$

Table 3.1: Summary of the complexity of each component of the split ACP algorithm.

uses plane wave expansion to discretize the Kohn-Sham equations. All calculations are carried out using the Berkeley Research Computing (BRC) High Performance Computing service. Each node consists of two Intel Xeon 10-core Ivy Bridge processors (20 cores per node) and 64 GB of memory.

4.1. 1D reduced Hartree-Fock model with nonlocal pseudopotential.

The 1D reduced Hartree-Fock model was introduced by Solovej [42], and has been used for analyzing defects in solids in e.g. [7, 8]. The simplified 1D model neglects the contribution of the exchange-correlation term. As discussed in previous sections, the presence of exchange-correlation functionals at LDA/GGA level does not lead to essential difficulties in phonon calculations. Furthermore, the nonlocal pseudopotential in the Kleinman-Bylander form [20] is added to this reduced model to test the availability for the split ACP to handle the case in presence of nonlocal potential.

The Hamiltonian in our 1D reduced Hartree-Fock model is given by

$$H[\rho] = -\frac{1}{2} \frac{d^2}{dx^2} + \left[\int K(x, y) (\rho(y) + m(y)) dy \right] \delta(x, x') + \gamma \sum_I b(x - R_I) b^*(x' - R_I). \quad (4.1)$$

Here $m(x) = \sum_I m_I(x - R_I)$ is the summation of pseudocharges. Each function $m_I(x)$ takes the form of a one-dimensional Gaussian

$$m_I(x) = -\frac{Z_I}{\sqrt{2\pi\sigma_I^2}} \exp\left(-\frac{x^2}{2\sigma_I^2}\right), \quad (4.2)$$

where Z_I is an integer representing the charge of the I -th nucleus. In our numerical simulation, we choose all σ_I to be the same.

Instead of using a bare Coulomb interaction which diverges in 1D when x is large, we use a Yukawa kernel as the regularized Coulomb kernel

$$K(x, y) = \frac{2\pi e^{-\kappa|x-y|}}{\kappa\epsilon_0}, \quad (4.3)$$

which satisfies the equation

$$-\frac{d^2}{dx^2}K(x, y) + \kappa^2 K(x, y) = \frac{4\pi}{\epsilon_0}\delta(x - y). \quad (4.4)$$

As $\kappa \rightarrow 0$, the Yukawa kernel approaches the bare Coulomb interaction given by the Poisson equation. The parameter ϵ_0 is used so that the magnitude of the electron static contribution is comparable to that of the kinetic energy. The ion-ion repulsion energy E_{II} is also computed using the Yukawa interaction K in the model systems.

The last term in $H[\rho]$ represents the kernel of the nonlocal pseudopotential, which is the summation of rank-1 real symmetric operator with real valued function

$$b(x) = \frac{1}{\sqrt{2\pi\sigma_b^2}} \exp\left(-\frac{x^2}{2\sigma_b^2}\right). \quad (4.5)$$

γ is a scaling factor used to control the magnitude of the nonlocal pseudopotential, which is, in practice, much smaller than the local pseudopotential.

The parameters used in this model are chosen as follows. Atomic units are used throughout the discussion unless otherwise mentioned. For all systems tested in this subsection, the distance between each atom and its nearest neighbor is set to 2.4 a.u. The Yukawa parameter $\kappa = 0.1$. The nuclear charge Z_I is set to 1 for all atoms, and σ_I is set to 0.3. The parameter ϵ_0 is chosen to be 80 so that the reduced Hartree-Fock model can be tuned to resemble a metallic system. In the nonlocal pseudopotential, the scaling factor $\gamma = -0.01$, as well as σ_b set to be 0.1 (this will cause the total energy to change by 1.47%). The temperature T is set to be 5000 K to emphasize the influence of partial occupation. The Hamiltonian operator is represented in a plane wave basis set.

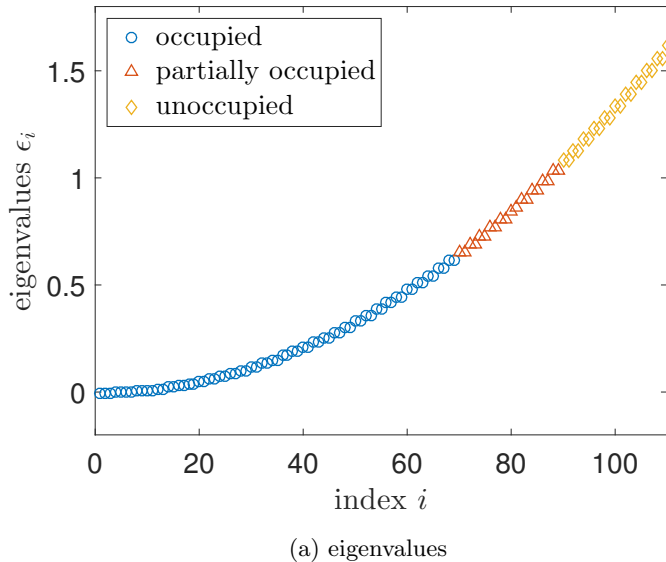


Fig. 4.1: Eigenvalues of the 1D system with $N_A = 80$.

For the system of size $N_A = 80$, the 110 smallest eigenvalues are shown in Fig. 4.1, and the corresponding occupational status near the chemical potential is shown in Fig. 3.1. There is no evident energy gap within the spectrum of the Hamiltonian. Orbitals can be partially occupied due to the finite temperature. Specifically, we identify an orbital to be (fully) occupied if the occupation number $f_i > 1 - 10^{-6}$, unoccupied if $f_i < 10^{-6}$, otherwise partially occupied. In this case, there are 20 partially occupied orbitals, whose eigenvalues are around the chemical potential. The total number of (fully) occupied and partially occupied orbitals N_{occ} is 89, and we choose $N_{\text{cut}} = N_{\text{occ}}$ for all the split ACP computations. Also we fix the number of pole expansion nodes N_p to be 40 unless otherwise mentioned.

In the ground state calculation, we use Anderson mixing [2] for accelerating the self-consistent field (SCF) iterations, and the linearized eigenvalue problems are solved by using the locally optimal block preconditioned conjugate gradient (LOBPCG) solver [21]. In DFPT, we use MINRES [37] to solve the Sternheimer equations iteratively. The initial guess vectors for the solutions are obtained from previous iterations in the Dyson equation to reduce the number of matrix-vector multiplications. The same strategy for choosing the initial guess is implemented for the split ACP formulation as well. Anderson mixing is used to accelerate the convergence of Dyson equations in DFPT, and in split ACP we use the fixed point iteration with Sherman-Morrison-Woodbury formula.

All numerical results of the split ACP method and FD approach below are benchmarked with results obtained from DFPT. We test the accuracy of the split ACP method in three different level: the diagonal elements $\text{diag}(\mathfrak{X}_0\mathbf{g})$, the diagonal elements of solution to Dyson equations $\text{diag}(\mathfrak{X}\mathbf{g})$, and the phonon frequencies $\{\omega_k\}$. For the diagonal elements $\text{diag}(\mathfrak{X}_0\mathbf{g})$ and $\text{diag}(\mathfrak{X}\mathbf{g})$, we directly measure the relative L^2 error, defined as $\|\text{diag}(\mathfrak{X}_0\mathbf{g}) - \text{diag}(\tilde{\mathfrak{X}}_0\mathbf{g})\|_2 / \|\text{diag}(\mathfrak{X}_0\mathbf{g})\|_2$. For the phonon frequencies, due to the presence of acoustic phonon modes for which ω_k is close to 0, instead of the relative error, we measure the absolute L^∞ error defined as $\max_k |\omega_k - \tilde{\omega}_k|$, where $\tilde{\omega}_k$ is obtained from FD or split ACP. We also demonstrate the efficiency of the split ACP method by comparing the computational time and scaling of split ACP with that of DFPT and FD.

$N_c \backslash N_\mu$	$3N_{\text{occ}}$	$4N_{\text{occ}}$	$5N_{\text{occ}}$	$6N_{\text{occ}}$	$7N_{\text{occ}}$	$8N_{\text{occ}}$
3	2.38E-02	2.17E-02	2.13E-02	2.12E-02	2.12E-02	2.12E-02
4	2.06E-02	9.43E-03	6.25E-03	6.21E-03	6.21E-03	6.21E-03
5	2.01E-02	7.88E-03	2.86E-03	2.85E-03	2.84E-03	2.84E-03
6	1.64E-02	6.76E-03	1.73E-03	1.65E-03	1.65E-03	1.65E-03
7	1.65E-02	9.30E-03	8.10E-04	6.85E-04	6.87E-04	6.87E-04
8	1.62E-02	9.07E-03	5.86E-04	2.53E-04	2.50E-04	2.50E-04
9	1.81E-02	7.24E-03	7.86E-04	1.51E-04	1.47E-04	1.47E-04
10	1.49E-02	6.53E-03	5.83E-04	7.99E-05	7.24E-05	7.24E-05

Table 4.1: The relative L^2 error $\|\text{diag}(\mathfrak{X}_0\mathbf{g}) - \text{diag}(\tilde{\mathfrak{X}}_0\mathbf{g})\|_2 / \|\text{diag}(\mathfrak{X}_0\mathbf{g})\|_2$ for $\tilde{N}_{\text{cut}}/N_{\text{cut}} \approx 1.06$ with the effective gap $\tilde{\varepsilon}_g/|\mathcal{I}| \approx 0.1408$.

In Table 4.1 and 4.2, we calibrate the accuracy of the split compression with different choices of the numbers of Chebyshev nodes N_c and the numbers of columns

$N_c \backslash N_\mu$	$3N_{\text{occ}}$	$4N_{\text{occ}}$	$5N_{\text{occ}}$	$6N_{\text{occ}}$	$7N_{\text{occ}}$	$8N_{\text{occ}}$
3	1.56E-02	8.52E-03	9.45E-04	7.42E-04	7.39E-04	7.39E-04
4	1.72E-02	7.79E-03	6.82E-04	1.02E-04	9.67E-05	9.67E-05
5	1.74E-02	9.49E-03	8.90E-04	6.00E-05	2.50E-05	2.50E-05
6	1.56E-02	7.80E-03	5.89E-04	7.06E-05	5.40E-06	5.38E-06
7	1.62E-02	9.07E-03	6.11E-04	5.51E-05	8.45E-07	8.42E-07
8	1.61E-02	9.04E-03	5.97E-04	4.73E-05	5.55E-07	3.21E-07
9	1.85E-02	9.08E-03	6.45E-04	4.52E-05	4.88E-07	3.20E-07
10	1.55E-02	9.52E-03	8.12E-04	5.72E-05	4.97E-07	3.20E-07

Table 4.2: The relative L^2 error $\|\text{diag}(\mathfrak{X}_0\mathfrak{g}) - \text{diag}(\tilde{\mathfrak{X}}_0\mathfrak{g})\|_2 / \|\text{diag}(\mathfrak{X}_0\mathfrak{g})\|_2$ for $\tilde{N}_{\text{cut}}/N_{\text{cut}} \approx 1.28$ with the effective gap $\tilde{\varepsilon}_g/|\mathcal{I}| \approx 0.6777$.

N_μ , for two different choices of \tilde{N}_{cut} , respectively. We measure the accuracy by relative L^2 error $\|\text{diag}(\mathfrak{X}_0\mathfrak{g}) - \text{diag}(\tilde{\mathfrak{X}}_0\mathfrak{g})\|_2 / \|\text{diag}(\mathfrak{X}_0\mathfrak{g})\|_2$, and choose $N_\mu = lN_{\text{occ}}$ where $l = 3, 4, \dots, 8$. Table 4.1 and 4.2 both show that, with a fixed number of Chebyshev nodes N_c , the error decreases monotonically with respect to N_μ , until limited by the accuracy of the Chebyshev interpolation procedure. Similarly, with a fixed number of selected columns, the numerical accuracy improves as more Chebyshev nodes are used in interpolation until limited by the choice of N_μ . Comparing Table 4.2 with Table 4.1, we also find that numerical accuracy can be better with a larger \tilde{N}_{cut} . This is due to the increase of the effective energy gap $\tilde{\varepsilon}_g$, which leads to a smaller numerical error in the Chebyshev interpolation procedure. For $\tilde{N}_{\text{cut}}/N_{\text{cut}} \approx 1.28$, the relative L^2 error of $\chi_0 G$ can be less than 10^{-6} for large enough N_c and N_μ .

We further study how different choices of N_c and \tilde{N}_{cut} affect the computational accuracy on $\text{diag}(\mathfrak{X}_0\mathfrak{g})$. Here for all N_c and \tilde{N}_{cut} , N_μ is fixed to be $480 \approx 5.4N_{\text{occ}}$ or $560 \approx 6.3N_{\text{occ}}$. This is determined the same way as that in the regular ACP formulation so that $|\tilde{R}_{N_\mu+1, N_\mu+1}| < \epsilon |\tilde{R}_{1,1}| \leq |\tilde{R}_{N_\mu, N_\mu}|$ in Algorithm 2 in [27], with $\epsilon = 10^{-4}$ and 10^{-5} , respectively. Fig. 4.2 compares the relative L^2 errors $\|\text{diag}(\mathfrak{X}_0\mathfrak{g}) - \text{diag}(\tilde{\mathfrak{X}}_0\mathfrak{g})\|_2 / \|\text{diag}(\mathfrak{X}_0\mathfrak{g})\|_2$ under different \tilde{N}_{cut} and N_c . We find that it can be sufficient to choose $\tilde{N}_{\text{cut}} \leq 2N_{\text{cut}}$ to achieve the best accuracy possible where further improvement is hindered by the the choice of N_μ (around 3×10^{-5} for $N_\mu \approx 5.4N_{\text{occ}}$ and 1×10^{-6} for $N_\mu \approx 6.3N_{\text{occ}}$). Under the split ACP formulation, the number of Chebyshev nodes is significantly reduced. Specifically, 4-8 nodes can already perform fairly accurate calculation while no less than 20 nodes are needed in the regular ACP formulation. Furthermore, the more Chebyshev nodes are used, the smaller \tilde{N}_{cut} we can choose to achieve the same accuracy. For example, if 5 nodes are adopted in Chebyshev interpolation, we need to choose \tilde{N}_{cut} as large as $1.55N_{\text{cut}}$ to achieve the best accuracy, while $\tilde{N}_{\text{cut}} \approx 1.2N_{\text{cut}}$ is sufficient if N_c increases to 8.

In order to demonstrate the effectiveness of the split representation, the relative L^2 error $\|\text{diag}(\mathfrak{X}\mathfrak{g}) - \text{diag}(\tilde{\mathfrak{X}}\mathfrak{g})\|_2 / \|\text{diag}(\mathfrak{X}\mathfrak{g})\|_2$ during the fixed point iteration when solving Dyson equation is shown in Fig. 4.3. For each choice of N_μ , numerical results show significant improvement after only one iteration, and the self-consistent iteration converges within two steps. After convergence, the error is around 1.4×10^{-3} for $\epsilon = 10^{-3}$, 6.2×10^{-5} for $\epsilon = 10^{-4}$, and 6.4×10^{-6} for $\epsilon = 10^{-5}$.

Next we compare the split ACP with DFPT and FD in terms of the accuracy of

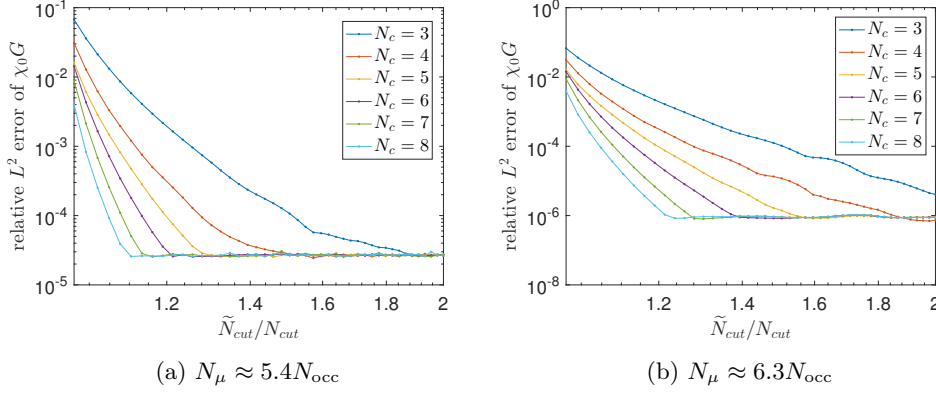


Fig. 4.2: The relative L^2 errors $\|\text{diag}(\tilde{\mathfrak{X}}_0 \mathfrak{g}) - \text{diag}(\tilde{\mathfrak{X}}_0 \mathfrak{g})\|_2 / \|\text{diag}(\tilde{\mathfrak{X}}_0 \mathfrak{g})\|_2$ under different \tilde{N}_{cut} and N_c

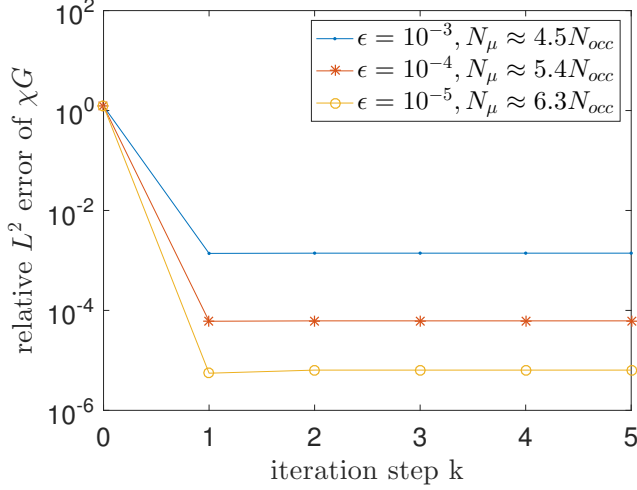


Fig. 4.3: Convergence for solving the Dyson equation using the split ACP formulation.

phonon frequencies. Table 4.3 presents L^∞ error of the phonon spectrum obtained by FD and split ACP with different parameters benchmarked with that from DFPT. In the FD approach, the convergence tolerance for LOBPCG is set to be 10^{-8} , and the SCF convergence tolerance is 10^{-10} . δ denotes the perturbation of each atom position to the origin. We remark that further smaller δ can lead to slightly larger numerical error due to the numerical instability of FD approach, and the numerical error of FD approach is usually around 10^{-4} . As for the split ACP, the same parameters for LOBPCG and SCF are chosen to converge the ground state calculation, and 5 nodes are used in the Chebyshev interpolation procedure. We find that it is sufficient to choose $N_p = 20$ and $N_\mu \approx 5.4N_{occ}$ to achieve comparable accuracy with FD approach.

Method and parameters	L^∞ -norm error
FD, $\delta = 0.01$	7.79E-05
split ACP, $N_p = 20$, $N_\mu \approx 5.4N_{\text{occ}}$ for $\epsilon = 10^{-4}$	5.90E-05
split ACP, $N_p = 40$, $N_\mu \approx 6.3N_{\text{occ}}$ for $\epsilon = 10^{-5}$	1.51E-05

Table 4.3: L^∞ error of the phonon frequencies. System size is $N_A = 80$. Chebyshev nodes $N_c = 5$ in split ACP.

Furthermore, with more nodes in pole expansion and more selected columns, the L^∞ error of split ACP can be as small as around 10^{-5} , in which case split ACP can be more accurate than FD approach.

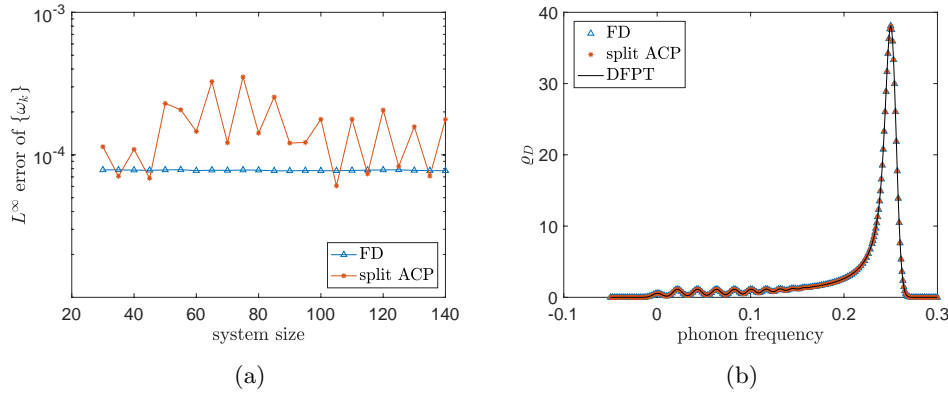


Fig. 4.4: (a) L^∞ error of the phonon frequencies $\{\omega_k\}$. (b) Phonon spectrum for the 1D system.

Method	Computational scaling
DFPT	4.0036
FD	3.8057
split ACP	3.1587

Table 4.4: Computational scaling measured from $N_A = 90$ to $N_A = 140$.

In the end we perform phonon calculations for systems of size from 30 to 140. We choose $\delta = 0.01$ for FD approach. Fig. 4.4a shows that the accuracy of phonon spectrum (L^∞ error) from FD approach remains roughly the same as the system size increases, which is empirically around 10^{-4} . For the split ACP, we find that $\epsilon = 10^{-4}$, $N_c = 4$, $N_p = 20$ and $N_{\text{cut}} \approx 1.7N_{\text{cut}}$ is sufficient to achieve error around 10^{-4} . Fig. 4.4b reports the phonon spectrum ρ_D for system of size $N_A = 140$. We remark that Fig 4.4b plots ρ_D by smearing the Dirac- δ distribution in (2.10) using a

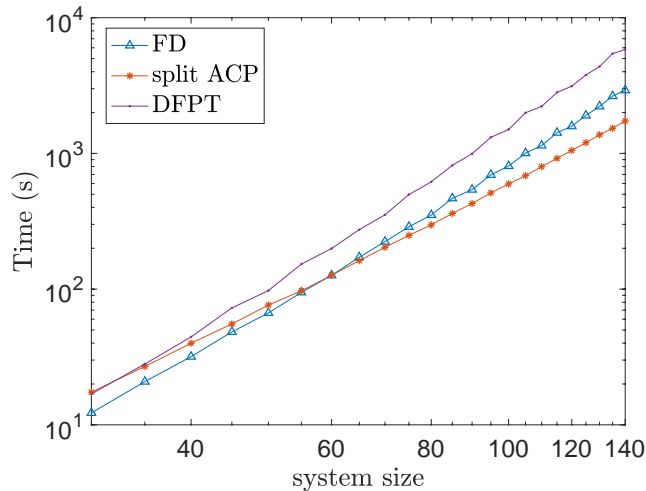


Fig. 4.5: Computational time of 1D examples.

regularized function

$$\delta_\sigma(x) = \frac{1}{\sqrt{2\pi\sigma^2}} e^{-\frac{x^2}{2\sigma^2}},$$

where the smear parameter σ is chosen to be 0.005.

To demonstrate the efficiency of the split ACP formulation, Fig. 4.5 compares the computational time of different methods. We observe that the split ACP can be more advantageous than DFPT for systems merely beyond 40 atoms, and become more advantageous than FD for systems beyond 60 atoms. For the largest system with 140 atoms, split ACP is 3.37 and 1.68 times faster than DFPT and FD, respectively.

Table 4.4 measures the slope of the computational cost with respect to system sizes from $N_A = 90$ to $N_A = 140$. In theory, the asymptotic computational cost of DFPT and FD should be $\mathcal{O}(N_e^4)$, and the cost of split ACP should be $\mathcal{O}(N_e^3)$. For all the methods, numerical scalings shown in Table 4.4 match closely with the theoretical ones.

4.2. 3D aluminum cluster. In this section, we present the result of phonon calculations of a 3D aluminum cluster. Each unit cell is a $7.65 \times 7.65 \times 7.65$ a.u. with 4 Al atoms. The computational supercell consists of $2 \times 2 \times 1$ unit cells and has 16 atoms and 48 electrons. We use the spin-restricted formulation and the Perdew-Zunger pseudopotential [39], and the temperature is set to 1000K. E_{cut} is set to 10 Hartree. We set $N_{\text{cut}} = 33$, $\tilde{N}_{\text{cut}} = 47$, and the number of Chebyshev interpolation N_c to be 6. For the system size tested, we found that using Eq.(3.1) directly for computing the singular part of the polarizability matrix much more faster than using the pole expansion. So the computation is done using Eq.(3.1) for the purpose of testing the accuracy of the algorithm. This results in much shorter computational time given the size of the system tested is small.

Figure 4.6 reports the relative error in the iteration of solving the Dyson equation. We remark that for this system, $N_\mu = 1584$. In comparison, the total grid points in

the discretization is $N_g = 42592$. This means that the numerical rank of the operator χ is far less than the number of grid points. The iteration is converged to 10^{-6} relative error for 6 steps.

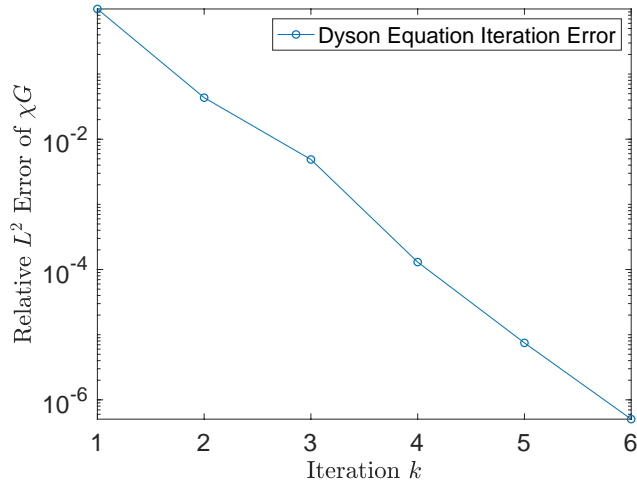


Fig. 4.6: The Dyson Equations iteration error.

Figure 4.7 reports the phonon spectrum computed from both FD and split ACP. The smearing parameter for plotting the spectrum is chosen as 0.008. The L^∞ error on the density of states is $5.62\text{E-}05$.

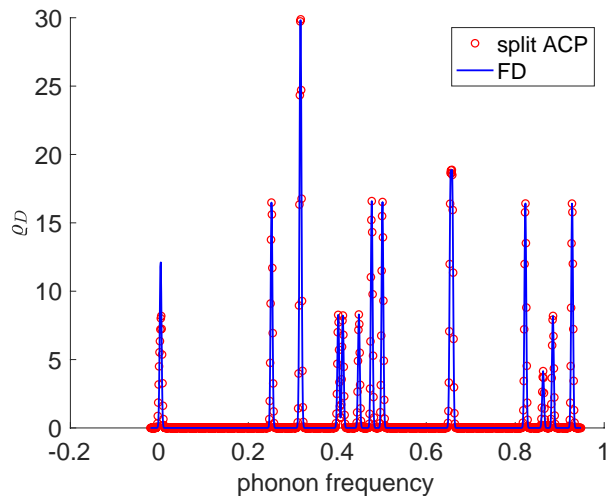


Fig. 4.7: Phonon spectrum of 3D Aluminum Cluster.

We remark that the purpose of the test above is to illustrate that the split ACP formulation can indeed be used to accurately obtain the phonon spectrum for 3D

metallic systems, with fractionally occupied states and nonlocal pseudopotentials. However, due to the small system size, the computational time of the split representation of ACP is in fact much longer than that of FD. Also we remark that there is difficulty in the DFPT approach in 3D. The Sternheimer equations are ill-conditioned and the MINRES iteration fail to converge. This result also emphasizes the necessity of introducing the effective gap in the split ACP.

Since KSSOLV is only designed to solve Kohn-Sham equations for systems with relatively small sizes, our implementation cannot reveal the efficiency of the split ACP approach yet for 3D systems, and this will be our future work.

5. Conclusion. We have introduced the split representation of a recently developed method called the adaptively compressed polarizability operator. The split ACP formulation incorporates nonlocal pseudopotentials and finite temperature effects successfully, hence generalizes the ACP formulation to solve for phonons in metallic systems as well. Our numerical results for model problems indicate that the computational advantage of the split ACP formulation can be clearly observed compared to DFPT and finite difference, even for systems of relatively small sizes. The numerical example for 3D Aluminum cluster shows that accuracy of the split ACP formulation in the application for computing the phonon spectrum for real materials.

The new split representation of ACP provides a systematic and complete solution to treating systems at finite temperature. We have used phonon calculation as an example to demonstrate the effectiveness as well as accuracy of the split representation of adaptively compressed polarizability operator. The same strategy can be applied to applications of DFPT other than phonon calculations, when the polarizability operator χ needs to be applied to a large number of vectors. Moreover, Meanwhile, all numerical tests are on single-threaded. Parallelized implementation would help fully test whether split representation of ACP formulation can achieve the goal of reducing complexity to asymptotically $\mathcal{O}(N_e^3)$. We will present the parallel implementation in the future.

Acknowledgments. This work was partially supported by the National Science Foundation under Grant No. DMS-1652330 (D. A. and L. L.), the U.S. Department of Energy under Contract No. de-sc0017867 (L. L. and Z. X.), and the U.S. Department of Energy under the Center for Applied Mathematics for Energy Research Applications (CAMERA) program (L. L.). We thank Berkeley Research Computing for the computational resources.

Appendix A. Using the Cauchy contour integral formulation, the density matrix at finite temperature can be represented as

$$P_0 = \frac{1}{2\pi i} \oint_{\mathcal{C}} f(z)(z - H)^{-1} dz. \quad (5.1)$$

When the Hamiltonian is perturbed to $H_\varepsilon = H_0 + \varepsilon \mathbf{g}$, and when ε is small enough, the perturbed density matrix P_ε can still be computed as

$$P_\varepsilon = \frac{1}{2\pi i} \oint_{\mathcal{C}} f(z)(z - H_\varepsilon)^{-1} dz. \quad (5.2)$$

Then we have

$$\begin{aligned}
P_\varepsilon - P_0 &= \frac{1}{2\pi i} \oint_{\mathcal{C}} f(z) [(z - H_\varepsilon)^{-1} - (z - H)^{-1}] dz \\
&= \frac{1}{2\pi i} \oint_{\mathcal{C}} f(z) [(z - H_\varepsilon)^{-1} \varepsilon \mathbf{g} (z - H)^{-1}] dz \\
&= \frac{1}{2\pi i} \oint_{\mathcal{C}} f(z) [(z - H)^{-1} \varepsilon \mathbf{g} (z - H)^{-1}] dz + \mathcal{O}(\varepsilon^2).
\end{aligned} \tag{5.3}$$

Hence by the definition of \mathfrak{X}_0 , we have

$$\mathfrak{X}_0 \mathbf{g} = \frac{1}{2\pi i} \oint_{\mathcal{C}} f(z) [(z - H)^{-1} \mathbf{g} (z - H)^{-1}] dz. \tag{5.4}$$

Using the spectral decomposition of H , and use the contour integral formulation

$$\begin{aligned}
\mathfrak{X}_0 \mathbf{g} &= \frac{1}{2\pi i} \oint_{\mathcal{C}} \sum_{j,k=1}^{\infty} f(z) \left[\frac{\psi_j \psi_j^* \mathbf{g} \psi_k \psi_k^*}{(z - \varepsilon_j)(z - \varepsilon_k)} \right] dz \\
&= \frac{1}{2\pi i} \sum_{j,k=1}^{\infty} \oint_{\mathcal{C}} dz \frac{f(z)}{(z - \varepsilon_j)(z - \varepsilon_k)} [\psi_j \psi_j^* \mathbf{g} \psi_k \psi_k^*] \\
&= \sum_{j \neq k}^{\infty} \frac{f_j - f_k}{\varepsilon_j - \varepsilon_k} [\psi_j \psi_j^* \mathbf{g} \psi_k \psi_k^*] + \sum_j^{\infty} f'_j [\psi_j \psi_j^* \mathbf{g} \psi_j \psi_j^*] \\
&= \sum_{j,k}^{\infty} \frac{f_j - f_k}{\varepsilon_j - \varepsilon_k} [\psi_j \psi_j^* \mathbf{g} \psi_k \psi_k^*],
\end{aligned} \tag{5.5}$$

where the $\frac{f_j - f_k}{\varepsilon_j - \varepsilon_k}$ is interpreted as the derivative when $j = k$.

For the purpose of computing singular part with contour representation, we have

$$\begin{aligned}
\mathfrak{X}_0^{(s)} \mathbf{g} &= \sum_{i=1}^{N_{\text{cut}}} \sum_{a=N_{\text{cut}}+1}^{\tilde{N}_{\text{cut}}} \frac{f_a - f_i}{\varepsilon_a - \varepsilon_i} \psi_a (\psi_a^* \mathbf{g} \psi_i) \psi_i^* + \text{h.c.} \\
&+ \sum_{i=1}^{N_{\text{cut}}} \sum_{a=1}^{N_{\text{cut}}} \frac{f_a - f_i}{\varepsilon_a - \varepsilon_i} \psi_a (\psi_a^* \mathbf{g} \psi_i) \psi_i^* \\
&= \frac{1}{2\pi i} \oint_{\mathcal{C}} dz \sum_{i=1}^{N_{\text{cut}}} \sum_{a=N_{\text{cut}}+1}^{\tilde{N}_{\text{cut}}} \frac{f(z)}{(z - \varepsilon_a)(z - \varepsilon_i)} [\psi_a \psi_a^* \mathbf{g} \psi_i \psi_i^*] + \text{h.c.} \\
&+ \frac{1}{2\pi i} \oint_{\mathcal{C}} dz \sum_{i=1}^{N_{\text{cut}}} \sum_{a=1}^{N_{\text{cut}}} \frac{f(z)}{(z - \varepsilon_a)(z - \varepsilon_i)} [\psi_a \psi_a^* \mathbf{g} \psi_i \psi_i^*] \\
&= \frac{1}{2\pi i} \oint_{\mathcal{C}} f(z) (z - H_{c,2})^{-1} \mathbf{g} (z - H_{c,1})^{-1} dz + \text{h.c.} \\
&+ \frac{1}{2\pi i} \oint_{\mathcal{C}} f(z) (z - H_{c,1})^{-1} \mathbf{g} (z - H_{c,1})^{-1} dz,
\end{aligned} \tag{5.6}$$

where $H_{c,1} = \sum_{i=1}^{N_{\text{cut}}} \psi_i \varepsilon_i \psi_i^*$, $H_{c,2} = \sum_{i=N_{\text{cut}}+1}^{\tilde{N}_{\text{cut}}} \psi_i \varepsilon_i \psi_i^*$ are the Hamiltonian operators projected to the subspace spanned by the first N_{cut} states, and to the subspace spanned by the following $(\tilde{N}_{\text{cut}} - N_{\text{cut}})$ states, respectively.

REFERENCES

- [1] S. L. ADLER, *Quantum theory of the dielectric constant in real solids*, Phys. Rev., 126 (1962), pp. 413–420.
- [2] D. G. ANDERSON, *Iterative procedures for nonlinear integral equations*, J. Assoc. Comput. Mach., 12 (1965), pp. 547–560.
- [3] S. BARONI, S. DE GIRONCOLI, A. DAL CORSO, AND P. GIANNOZZI, *Phonons and related crystal properties from density-functional perturbation theory*, Rev. Mod. Phys., 73 (2001), pp. 515–562.
- [4] S. BARONI, P. GIANNOZZI, AND A. TESTA, *Green's-function approach to linear response in solids*, Phys. Rev. Lett., 58 (1987), pp. 1861–1864.
- [5] A. D. BECKE, *Density-functional exchange-energy approximation with correct asymptotic behavior*, Phys. Rev. A, 38 (1988), pp. 3098–3100.
- [6] D. R. BOWLER AND T. MIYAZAKI, *$O(N)$ methods in electronic structure calculations*, Rep. Prog. Phys., 75 (2012), p. 036503.
- [7] E. CANCÈS, A. DELEURENCE, AND M. LEWIN, *A new approach to the modeling of local defects in crystals: The reduced Hartree-Fock case*, Commun. Math. Phys., 281 (2008), pp. 129–177.
- [8] ———, *Non-perturbative embedding of local defects in crystalline materials*, J. Phys.: Condens. Matter, 20 (2008), pp. 294213–294218.
- [9] E. CANCES AND N. MOURAD, *A mathematical perspective on density functional perturbation theory*, Nonlinearity, 27 (2014), p. 1999.
- [10] D. M. CEPERLEY AND B. J. ALDER, *Ground state of the electron gas by a stochastic method*, Phys. Rev. Lett., 45 (1980), pp. 566–569.
- [11] T. F. CHAN AND PER C. HANSEN, *Computing truncated singular value decomposition least squares solutions by rank revealing QR-factorizations*, SIAM J. Sci. Stat. Comput., 11 (1990), pp. 519–530.
- [12] H. CHENG, Z. GIMBUTAS, P. G. MARTINSSON, AND V. ROKHLIN, *On the compression of low rank matrices*, SIAM J. Sci. Comput., 26 (2005), pp. 1389–1404.
- [13] D. FOERSTER, *Elimination, in electronic structure calculations, of redundant orbital products*, J. Chem. Phys., 128 (2008), p. 034108.
- [14] D. FRENKEL AND B. SMIT, *Understanding Molecular Simulation: From Algorithms to Applications*, Academic Press, 2002.
- [15] F. GIUSTINO, M. L. COHEN, AND S. G. LOUIE, *GW method with the self-consistent Sternheimer equation*, Phys. Rev. B, 81 (2010), p. 115105.
- [16] S. GOEDECKER, *Linear scaling electronic structure methods*, Rev. Mod. Phys., 71 (1999), pp. 1085–1123.
- [17] X. GONZE AND C. LEE, *Dynamical matrices, Born effective charges, dielectric permittivity tensors, and interatomic force constants from density-functional perturbation theory*, Phys. Rev. B, 55 (1997), p. 10355.
- [18] M. GU AND S. EISENSTAT, *Efficient algorithms for computing a strong rank-revealing qr factorization*, SIAM J. Sci. Comput., 17 (1996), pp. 848–869.
- [19] P. HOHENBERG AND W. KOHN, *Inhomogeneous electron gas*, Phys. Rev., 136 (1964), pp. B864–B871.
- [20] L. KLEINMAN AND D. M. BYLANDER, *Efficacious form for model pseudopotentials*, Phys. Rev. Lett., 48 (1982), pp. 1425–1428.
- [21] A. V. KNYAZEV, *Toward the optimal preconditioned eigensolver: Locally optimal block preconditioned conjugate gradient method*, SIAM J. Sci. Comp., 23 (2001), pp. 517–541.
- [22] W. KOHN, *Density functional and density matrix method scaling linearly with the number of atoms*, Phys. Rev. Lett., 76 (1996), pp. 3168–3171.
- [23] W. KOHN AND L. SHAM, *Self-consistent equations including exchange and correlation effects*, Phys. Rev., 140 (1965), pp. A1133–A1138.
- [24] C. LEE, W. YANG, AND R. G. PARR, *Development of the Colle-Salvetti correlation-energy formula into a functional of the electron density*, Phys. Rev. B, 37 (1988), pp. 785–789.
- [25] L. LIN, J. LU, L. YING, AND W. E, *Pole-based approximation of the Fermi-Dirac function*, Chin. Ann. Math., 30B (2009), p. 729.
- [26] L. LIN, Y. SAAD, AND C. YANG, *Approximating spectral densities of large matrices*, SIAM Rev., 58 (2016), p. 34.
- [27] L. LIN, Z. XU, AND L. YING, *Adaptively compressed polarizability operator for accelerating large scale ab initio phonon calculations*, Multiscale Model. Simul., 15 (2017), pp. 29–55.
- [28] J. LU, C. D. SOGGE, AND S. STEINERBERGER, *Approximating pointwise products of Laplacian eigenfunctions*, 2018. preprint, arXiv:1811.10447.
- [29] J. LU AND L. YING, *Compression of the electron repulsion integral tensor in tensor hypercon-*

- traction format with cubic scaling cost, *J. Comput. Phys.*, 302 (2015), p. 329.
- [30] R. MARTIN, *Electronic Structure – Basic Theory and Practical Methods*, Cambridge Univ. Pr., West Nyack, NY, 2004.
- [31] N.D. MERMIN, *Thermal properties of the inhomogeneous electron gas*, *Phys. Rev.*, 137 (1965), p. A1441.
- [32] JONATHAN E MOUSSA, *Minimax rational approximation of the fermi-dirac distribution*, *The Journal of chemical physics*, 145 (2016), p. 164108.
- [33] YUJI NAKATSUKASA, OLIVIER SÈTE, AND LLOYD N TREFETHEN, *The aaa algorithm for rational approximation*, *SIAM Journal on Scientific Computing*, 40 (2018), pp. A1494–A1522.
- [34] H.-V. NGUYEN, T. A. PHAM, D. ROCCA, AND G. GALLI, *Improving accuracy and efficiency of calculations of photoemission spectra within the many-body perturbation theory*, *Phys. Rev. B*, 85 (2012), p. 081101.
- [35] A. M. N. NIKLASSON AND M. CHALLACOMBE, *Density matrix perturbation theory*, *Phys. Rev. Lett.*, 92 (2004), p. 193001.
- [36] G. ONIDA, L. REINING, AND A. RUBIO, *Electronic excitations: density-functional versus many-body Green’s-function approaches*, *Rev. Mod. Phys.*, 74 (2002), p. 601.
- [37] C. C. PAIGE AND M. A SAUNDERS, *Solution of sparse indefinite systems of linear equations*, *SIAM J. Numer. Anal.*, 12 (1975), pp. 617–629.
- [38] J. P. PERDEW, K. BURKE, AND M. ERNZERHOF, *Generalized gradient approximation made simple*, *Phys. Rev. Lett.*, 77 (1996), pp. 3865–3868.
- [39] J. P. PERDEW AND A. ZUNGER, *Self-interaction correction to density-functional approximations for many-electron systems*, *Phys. Rev. B*, 23 (1981), pp. 5048–5079.
- [40] X. REN, P. RINKE, V. BLUM, J. WIEFERINK, A. TKATCHENKO, A. SANFILIPPO, K. REUTER, AND M. SCHEFFLER, *Resolution-of-identity approach to Hartree–Fock, hybrid density functionals, RPA, MP2 and GW with numeric atom-centered orbital basis functions*, *New J. Phys.*, 14 (2012), p. 053020.
- [41] A. SODT, J. E. SUBOTNIK, AND M. HEAD-GORDON, *Linear scaling density fitting*, *J. Chem. Phys.*, 125 (2006), p. 194109.
- [42] J. P. SOLOVEJ, *Proof of the ionization conjecture in a reduced Hartree-Fock model*, *Invent. Math.*, 104 (1991), pp. 291–311.
- [43] P. UMARI, G. STENUIT, AND S. BARONI, *Optimal representation of the polarization propagator for large-scale GW calculations*, *Phys. Rev. B*, 79 (2009), p. 201104.
- [44] ———, *GW quasiparticle spectra from occupied states only*, *Phys. Rev. B*, 81 (2010), p. 115104.
- [45] F. WEIGEND, *A fully direct RI-HF algorithm: Implementation, optimised auxiliary basis sets, demonstration of accuracy and efficiency*, *Phys. Chem. Chem. Phys.*, 4 (2002), pp. 4285–4291.
- [46] N. WISER, *Dielectric constant with local field effects included*, *Phys. Rev.*, 129 (1963), pp. 62–69.
- [47] F. WOOLFE, E. LIBERTY, V. ROKHLIN, AND M. TYGERT, *A fast randomized algorithm for the approximation of matrices*, *Appl. Comput. Harmon. Anal.*, 25 (2008), pp. 335–366.
- [48] C. YANG, J. C. MEZA, B. LEE, AND L. W. WANG, *KSSOLV—a MATLAB toolbox for solving the Kohn–Sham equations*, *ACM Trans. Math. Software*, 36 (2009), p. 10.